Applied Ocean Research 123 (2022) 103176

Contents lists available at ScienceDirect

Applied Ocean Research

journal homepage: www.elsevier.com/locate/apor

Hydrodynamic analysis of ship manoeuvrability in shallow water using high-fidelity URANS computations

Daejeong Kim *, Tahsin Tezdogan, Atilla Incecik

Department of Naval Architecture, Ocean and Marine Engineering, University of Strathclyde, 100 Montrose Street, Glasgow G4 0LZ, United Kingdom

ARTICLE INFO

Key words:
Computational fluid dynamics
RANS solver
Ship manoeuvrability
Shallow water
Manoeuvring hydrodynamic loads

ABSTRACT

The manoeuvring performance of a ship in shallow water is substantially different from its performance in deep water, attributed to shallow water effects caused by the presence of a finite water depth. Without a doubt a ship will navigate in areas of shallow water at various times during its operational life (such as when approaching harbours or ports), which underscores the importance of understanding the shallow water effects on ship manoeuvrability. In the present paper, the manoeuvrability of the KRISO Container Ship (KCS) model in different shallow water conditions was comprehensively analysed by means of the unsteady Reynolds-Averaged Navier-Stokes (URANS) computations coupled with the equations of rigid body motion with full six degrees of freedom (6DOF). A dynamic overset grid approach was implemented to allow the ship hull to move in 6DOF in a computational domain and to enable the rudder to be deflected according to a rudder controller for free-running manoeuvres. A series of manoeuvring simulations were performed in shallow waters with water depth to draft ratios varying between 1.2 and 4.0, and partially validated with the available experimental data from a free running test. The numerical results revealed that the ship advance, transfer, and tactical diameter mainly increased with the decrease in the ratio of water depth to draft, closely associated with the complicated interactions between the hull wake, boundary layer, propeller, vortex, and sea floor.

1. Introduction

The trend of ever-increasing ship size has called for a need to understand the manoeuvring performance of a vessel in shallow water. Vessels will navigate in areas of shallow water at various times during their operational life, such as when approaching harbours or ports. As stated in Tezdogan et al. (2016), it is also true that some coastal waters and open sea areas can be regarded as shallow water regions in which the water depth is limited. Masters and navigation officers, who are in charge of ship handling with a high focus on navigation safety, should fully understand the manoeuvring capabilities of a ship in shallow water for proper decision-making about ship manoeuvring actions. In practice, however, they have only access to the manoeuvring information of their vessels in deep water, which is generally obtained by full-scale sea trials or model-scale experiments. This stems from the fact that evaluating the manoeuvring performance of a surface vessel in deep water practically becomes an industry standard in accordance with the International Maritime Organisation (IMO) standards for ship manoeuvrability (IMO, 2002). The IMO recommends that the water depth should exceed four times the mean draft of a ship when estimating manoeuvring behaviours. It is undeniable fact that the full-scale sea trial or model-scale experiment compliant with the IMO requirement can be informative in confirming a ship's manoeuvrability in deep unrestricted water. However, they are not able to provide a practical insight into the understanding of ship manoeuvrability in shallow water as the manoeuvring behaviour of a vessel in shallow water differs significantly from its behaviour in deep water. For this reason, this study aims to investigate the manoeuvring performance of a ship in shallow water, using an unsteady reynolds-averaged navier stokes (URANS) method.

There have been a number of previous studies examining the effects of finite depths on the manoeuvring performance of a ship. For example, the manoeuvring characteristics of the Esso Osaka in shallow water were investigated in Manoeuvring Committee in 21st ITTC, performing a series of model tests and full-scale sea trials (ITTC, 2002). In the investigation, it was demonstrated that the ship operating in shallow water experienced larger increases in the turning parameters (such as the ship advance, transfer, and tactical diameter) when compared to those measured in deep water. In addition, it was reported that the

* Corresponding author.
E-mail address: daejeong.kim@strath.ac.uk (D. Kim).

https://doi.org/10.1016/j.apor.2022.103176
Received 15 December 2021; Received in revised form 25 March 2022; Accepted 1 April 2022

contribution of propulsion to the later force and yawing moment acting on the ship is much more important in shallow water. According to Toxopeus et al. (2013), limited water depth has a remarkable influence on the performance of a ship, clearly demonstrated when the ratio of water depth to draft is less than 1.5. One of their key findings is that when a ship is operating at a drift angle, the forces and moments acting on the hull in shallow water increase considerably, compared to those measured in deep water. This implies that the presence of a finite water depth can lead to substantial changes in a ship's manoeuvrability when compared to deep water conditions, mainly being attributed to the strong interaction between the hull, propeller, and rudder with the sea floor. It is also worth noting that the Knowledge Centre for Manoeuvring in Shallow and Confined Water provides experimental-benchmark data sets for the manoeuvring performance of a ship in shallow water. The Knowledge Centre investigated the manoeuvring characteristics of the KVLCC2 and DTC in shallow water carrying out captive model tests in the framework of the European SHOPERA project (Papanikolaou et al., 2015), with particular attention to the presence of waves. In Carrica et al. (2016), an experimental and numerical study on the manoeuvrability of the KCS in shallow water was performed. They conducted a 20/5 modified zigzag manoeuvre in which the approach conditions are Fr (Froude number) = 0.095 and h/D (depth to draft ratio) = 1.2. Free-running tests were carried out in the shallow water towing tank at Flanders Hydraulics Research and free-running CFD simulations were performed with the ship hydrodynamics code REX, a merge of the codes CFDShip-Iowa v4.5. In their work, the comparison in terms of kinematic and dynamic parameters confirmed the satisfactory agreement between available experimental free-running tests and their CFD predictions. In addition, the principal properties of the flow field were described, with particular attention to the strong mutual interactions between the hull, the propeller, the rudder, and the tank bottom (the sea bed). Lee and Hong (2017) carried out numerical simulations to analyse the hydrodynamic forces and moments acting on the KVLCC2 and DTC in different shallow waters by means of a RANS solver. It was revealed that the hydrodynamic forces moments experienced by the ship remarkably increased as the ratio of water depth to draft decreased. Liu et al. (2019) performed the virtual pure sway tests of the DTC model in shallow water to determine hydrodynamic derivatives by means of a RANS solver; in their study, the effects of finite water depths on ship speed, dynamic sinkage were discussed.

In general, the evaluation of the manoeuvring performance of a vessel has been addressed by means of indirect or direct approaches. The indirect methods involve solving simplified mathematical models (e.g., Abkowitz model (Abkowitz, 1964) and manoeuvring modelling group (MMG) model (Inoue et al., 1981; Yasukawa and Yoshimura, 2015) for the prediction of the manoeuvring performance. In the indirect methods, the complete set of hydrodynamic coefficients need to be obtained from experiments, potential theory, or computational fluid dynamics (CFD). Despite the benefit that the indirect approach is incomparably fast in terms of computational time, the accuracy of simplified mathematical models strongly relies on the validity of hydrodynamic coefficients. Besides, the indirect methods are not capable of incorporating not only viscous effects but also the flow acceleration on the rudder caused by a rotating propeller, thereby limiting the applicability and accuracy of the simplified mathematical models. The direct methods are based on free-running tests in manoeuvring basins or free-running simulations in CFD, being capable of estimating a ship's manoeuvrability in a direct way. Model-scale free-running experiments have been perceived to be the most reliable approach in predicting the manoeuvring performance of a ship as they are the closest method to mimic real operating conditions. Experimental data, thanks to high reliability, are usually used as benchmark data sets for comparison with other approaches; however, it is quite costly and time-consuming to prepare a ship model equipped with a controllable rudder and propeller and arrange the facilities suited to the experiments.

Recently, advances in computational power and numerical algorithms have made it possible to directly predict the manoeuvring capabilities of a ship by performing free-running CFD simulations. CFD is progressively gaining popularity for manoeuvring prediction since it accounts for viscous and turbulent effects being important on ship manoeuvring as well as does not use any consumables (as opposed to experiments). In addition, free-running CFD simulations have remarkable advantages in providing very detailed results including surface elevations and velocity/pressure fields which lead to a better interpretation of the hydrodynamic phenomena occurring during the manoeuvre. Mofidi and Carrica (2014), who performed free-running CFD simulations for the KCS, state that CFD is a high-fidelity numerical method on the basis of physical principles and yields results that are typically accurate with almost no need for empirical inputs. Given the benefits of the CFD approach, it is believed that the direct CFD simulations of ship manoeuvring are very attractive alternatives to the indirect methods and experiments, providing a comprehensive description of a ship's manoeuvrability with much less expense.

Muscari et al. (2008), as the first researchers in the field of CFD applications for the direct prediction of ship manoeuvrability, implemented free-running CFD simulations using an unsteady Reynolds Averaged Navier-Stokes approach. In their studies, the turning behaviours of a self-propelled twin-screw patrol vessel in calm water were evaluated, where the flow field interaction between the ship hull and the propeller was taken into account by a simplified propeller model. In Mofidi and Carrica (2014) 10/10 and 15/1 zigzag manoeuvres of the KCS model with a moving rudder and rotating propeller were computed by utilising CFDShip-Iowa which is a piece of general purpose CFD software developed at the University of Iowa. The simulations were carried out at model scale in deep calm water, presenting comparisons against towing tank zigzag tests. Similar computations regarding free-running CFD manoeuvres in deep calm water were presented in Broglia et al. (2015); Shen et al. (2015); Dubbioso et al. (2016); Hasanvand and Hajivand (2019).

More recent work in this field has concentrated on free-running CFD simulations in waves, due to an increasing demand for the accurate evaluation of a ship's manoeuvrability in waves (IMO, 2014; ITTC, 2017). The investigation in Wang et al. (2017) was focused on the course keeping capabilities of the ONR Tumblehome ship in regular waves by carrying out direct CFD simulations which adopted the actual rotating propellers and moving rudders with no simplifications. Then, a series of studies on the manoeuvring behaviour of the ONR Tumblehome ship were performed, such as standard 10/10 zigzag manoeuvres in regular waves (Wang et al., 2018) and turning circle manoeuvres in regular waves (Wang and Wan, 2018). In Kim et al. (2021c) URANS simulations for the KCS performing turning circle manoeuvres in regular waves of different directions were reported; the agreement between the simulation results and available experimental data were satisfactory. Afterwards, similar URANS simulations were carried out by Kim et al. (2021a); Kim et al. (2021b); Kim et al. (2022); Kim and Tezdogan (2022) to evaluate the manoeuvring performance of the KCS in regular waves or irregular waves. Given the aforementioned literature on the direct CFD approach, CFD applications to ship manoeuvring studies (for example, course keeping, zigzag, and turning circle manoeuvres) seem promising, showing a satisfactory degree of accuracy for free-running CFD models.

Given the benefits of the direct CFD method, it is expected that the results obtained from free-running CFD simulations can provide a clear and detailed insight into the physical phenomena of a ship performing a self-propelled manoeuvre in shallow water. The global analysis of the complex fluid-structure interactions between the hull, rudder, propeller, and sea bed during manoeuvres can also be helpful for the analysis of experimental observations pertaining to a ship's performance in shallow water. So far, however, the previous studies related to free-running CFD simulations have mostly focused on the evaluation of a ship's manoeuvrability in deep waters as described above. In other words, the research devoted to investigating ship manoeuvrability in shallow water areas has been very limited in number and scope. Carrica et al. (2016), who

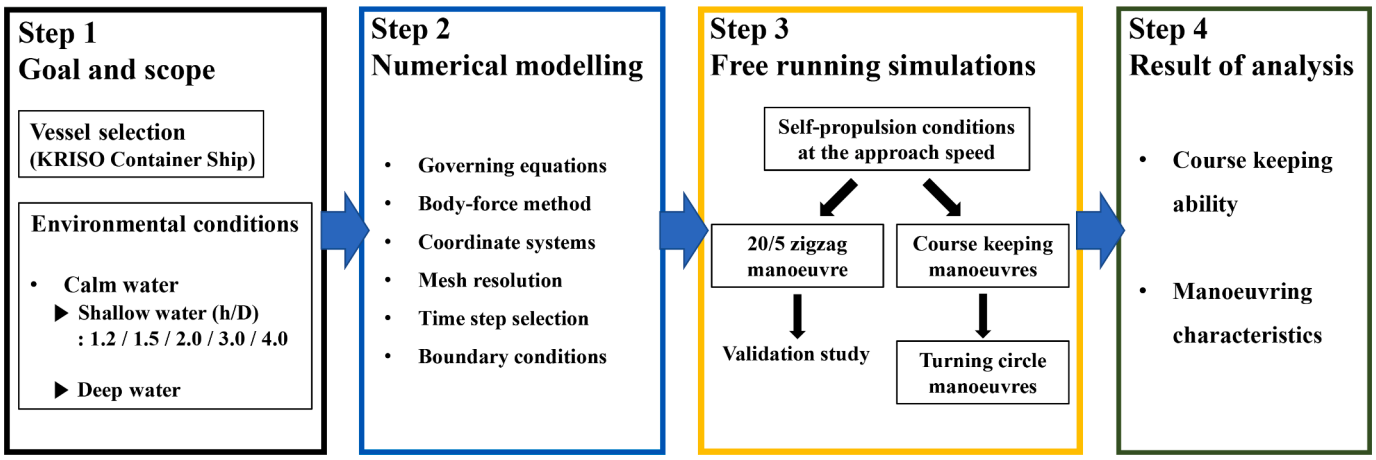

Fig. 1. Proposed research methodology for the CFD free-running simulations.

carried out a 20/5 zigzag manoeuvre for the KCS in shallow water using CFD, only focused on case-specific analyses with a single condition of $h/D = 1.2$, such that their findings are not able to provide the general observations on the relationship between finite depths and manoeuvring behaviours. Taking into account the lack of previous studies concerning ship manoeuvrability in shallow water by means of free-running CFD simulation, the research reported in this work was motivated to analyse the effect of different shallow waters on the manoeuvring behaviour of a ship. In addition, as discussed in detail by Kim et al. (2021b), performing analyses of the turning behaviour of ships is of great importance in ship navigation. To the best of our knowledge, there is no study in the literature addressing the course keeping and turning manoeuvres of a ship in shallow water by means of free-running CFD simulations. A decision was therefore made to investigate the course keeping and turning performance of a ship in the CFD simulations presented in this paper.

In the present work, the turning capabilities of the KCS model in different shallow waters are investigated. Comprehensive analyses are provided for the manoeuvring indices and hydrodynamic loads closely associated with the turning behaviours, and, in order to gain more insight in understanding the turning manoeuvres, the various hydrodynamic phenomena occurring during the manoeuvre (including velocity and pressure fields) are evaluated. This study therefore may be useful to understand the comprehensive manoeuvring behaviour of a container ship model in different shallow water areas.

This paper is organised as follows: in the next section, the research methodology adopted in this study is illustrated, with a detailed description of the procedure in the included sub-sections. Next, in Section 3, all of the CFD results from this work, including validation studies, are demonstrated and discussed in detail. Finally, Section 4 briefly summarises the main results drawn from this work, along with recommendations for future research.

2. Methodology

This section will outline the research methodology adopted in this work, along with a detailed explanation of the procedure in the contained sub-sections. In this study the manoeuvring behaviours of the KCS in different shallow waters were examined; to this purpose, a procedure was devised consisting of four steps: *1) goal and scope, 2) numerical modelling, 3) execution of free running simulations, and 4) results of analysis*. A flow chart representing the process is presented in Fig. 1. This procedure basically follows the methodology developed in the authors' previous work (Kim et al., 2021a) but has been revised according to the purpose and the scope of this research. As the first step in Fig. 1, this paper established the overall research aim and objective with the scope of the analysis. All aspects of numerical modelling associated with the free-running CFD model are given in the second step. In the third step, the free-running manoeuvres using the CFD model formulated on the basis of the previous steps are conducted. In the fourth step, all of the results obtained from the CFD simulations are illustrated and discussed, with particular emphasis on the relationship between the ship's turning performance and finite depths.

2.1. Step 1: goal and scope

Given the scarce previous research on ship manoeuvrability in shallow water, this paper is to provide a comprehensive understanding of the shallow water effects on the manoeuvring performance of the

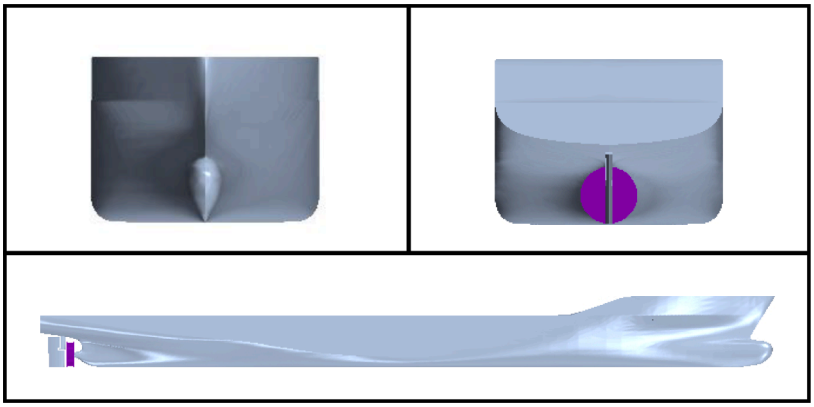

Fig. 2. KCS geometry with a semi balanced rudder and an actuator disk.

Table 1
The main particulars of the KCS model used in this study.

Main particulars	Symbols	Model scale (1:75.24)
Length between the perpendiculars	$L_{BP}(m)$	3.057
Length of waterline	$L_{WL}(m)$	3.0901
Beam at waterline	$B_{WL}(m)$	0.4280
Draft	D(m)	0.1435
Displacement	$\Delta(m^3)$	0.1222
Block coefficient	C_B	0.651
Ship wetted area with rudder	S (m^2)	1.6834
Longitudinal centre of buoyancy	$\%L_{BP}$, fwd+	−1.48
The metacentric height	GM(m)	0.008
Radius of gyration	K_{xx}/B	0.49
Radius of gyration	K_{yy}/L_{BP}, K_{zz}/L_{BP}	0.25
Propeller diameter	$D_P(m)$	0.105
Propeller rotation direction (view from stern)		Right hand side
Rudder turn rate	(deg/s)	20.1
Froude number	Fr	0.095
Reynolds number	Re	1.25×10^6

Table 2
The simulation cases to which the CFD model is applied.

Case	Surge speed U_0 (m/s)	Propeller rev. (RPS)	Depth/ draft h/D	Free running simulations
0	0.518	6.75	1.20	20/5 zigzag, starting to port (**Validation case**)
1	0.518	6.75	1.20	Course keeping, 35° starboard turn
2	0.518	6.56	1.50	Course keeping, 35° starboard turn
3	0.518	6.43	2.00	Course keeping, 35° starboard turn
4	0.518	6.28	3.00	Course keeping, 35° starboard turn
5	0.518	6.24	4.00	Course keeping, 35° starboard turn
6	0.518	6.07	Deep water	Course keeping, 35° starboard turn

ship. The specific objectives of this research include: (1) developing the CFD model for free-running manoeuvres in shallow water; (2) validating CFD computations against available experimental data in order to ensure a sufficient level of accuracy for the free-running CFD model; (3) carrying out numerical simulations for the selected test cases and analysing the shallow water effects on the ship manoeuvrability such as course keeping and turning capabilities; (4) making recommendations for future studies in particular consideration of the research limitations identified in the current work.

Numerical simulations were performed for the KCS model (a container ship developed by KRISO in Korea) displayed in Fig. 2. The ship model with a scale factor of 75.24 is appended with a semi-balanced rudder and an actuator disk, and the main characteristics of the model are reported in Table 1. Seven different cases to be simulated in CFD were taken into consideration within this study, as shown in Table 2 and Fig. 3 (each case indicated by their case numbers). In this study, a 20/5 modified zigzag manoeuvre (Case 0) was carried out in shallow water with water depth to draft ratio $h/D = 1.2$ for validation purposes. The experimental results of the 20/5 zigzag manoeuvre provided by MARIN (SIMMAN, 2020) were used as benchmark data for validation. In addition, two representative free-running manoeuvres (namely, course keeping and standard turning manoeuvres) were performed in different depth to draft ratios (Case 1 – 6): 1) $h/D = 1.2$, 2) $h/D = 1.5$, 3) $h/D = 2.0$, 4) $h/D = 3.0$, 5) $h/D = 4.0$, and 6) deep water. The first procedure for the free-running manoeuvres involved achieving self-propulsion at the approaching speed; the corresponding Froude and Reynolds numbers were $Fr = 0.095$ and $Re = 1.25 \times 10^6$, respectively. It should be noted that the approach speed was reached, the revolution speed of the actuator disk was kept constant at the self-propulsion value during the free-running manoeuvres to be performed. Then, the course-keeping manoeuvres were started from the stable state of the self-propulsion condition, based on a rudder controller that controls the rudder deflection angle to make the ship sail forward. Following this, the standard turning circle manoeuvres (35° starboard turns) were performed to evaluate the shallow water effects on the turning behaviour of the ship.

2.2. Step 2: numerical modelling

In this study, the computations were implemented by means of the commercial CFD package STAR-CCM+, version 15.04. The main features of the numerical approach applied are illustrated in this subsection.

2.2.1. Governing equations

The CFD solver employed in this work solves the URANS equations for unsteady turbulent flows around complex geometries. The continuity and momentum equations for an incompressible viscous fluid without body forces can be written in vectorial form as

$$\nabla\cdot\mathbf{U} = 0 \tag{1}$$

$$\frac{\partial(\rho\mathbf{U})}{\partial t} + \nabla\cdot\left[\rho(\mathbf{U}-\mathbf{U_g})\mathbf{U}\right] = -\nabla p + \nabla\cdot(\mu_{\text{eff}}\nabla\mathbf{U}) + \nabla\mathbf{U}\cdot\nabla\mu_{\text{eff}} + q_i \tag{2}$$

where $\mathbf{U}$ is the fluid velocity and $\mathbf{U_g}$ is the grid velocity; p is the static pressure; ρ is the fluid density; $\mu_{\text{eff}} = \rho(\nu+\nu_t)$ indicates the effective dynamic viscosity, where ν and ν_t represent the kinematic and eddy viscosity, respectively (ν_t is obtained from the turbulence model); q_i is a user-defined source term.

Three-dimensional free surface flows were modelled using a two-phase level set approach with the Volume of Fluid (VOF) method proposed by Hirt and Nichols (1981). The transport equation is expressed as follows (Siemens, 2020):

$$\frac{\partial\alpha_i}{\partial t} + \nabla\cdot\left[\alpha_i(\mathbf{U}-\mathbf{U_g})\right] = S_{\alpha_i} - \frac{\alpha_i}{\rho_i}\frac{D\rho_i}{Dt} - \frac{1}{\rho_i}\nabla\cdot(\alpha_i\rho_i\mathbf{v}_{d,i}) \tag{3}$$

in which α_i is the volume fraction of phase i and its value varies from 0 to 1 to describe the relative proportion of fluid in each cell ($\alpha = 0$: non-wetting phase (air), $0 < \alpha < 1$: two-phase interface (free surface), $\alpha = 1$: wetting phase (water)); S_{α_i} is a user-defined source term of phase i; $\frac{D\rho_i}{Dt}$ is the Lagrangian derivative of the phase densities ρ_i; $\mathbf{v}_{d,i}$ is the diffusion velocity. According to Perić and Abdel-Maksoud (2018), undesired wave reflections occurring at domain boundaries in flow simulations can be eliminated by applying source terms for the momentum equation (q_i) and the VOF transport equation (S_{α_i}).

The solver used is based on a finite volume method that discretises the Navier-Stokes equations. In the present work, the convection terms were discretised with a second-order upwind scheme while a second-order centred scheme was adopted for the diffusive terms. The turbulence model selected for the simulations was the Shear Stress Transport (SST) model (Menter, 1994) which blends the best features of the near-wall accuracy of the k-ω model and the free-stream accuracy of the k-ε model. Menter's SST model has been used in several previous studies regarding free-running CFD simulations (Mofidi and Carrica, 2014; Carrica et al., 2016; Wang and Wan, 2018; Liu et al., 2020; Kim et al., 2021c). The temporal discretisation was performed with a second-order implicit backward Euler scheme. SIMPLE (Semi-Implicit Method for Pressure-Linked Equations) was adopted for a segregated pressure-velocity coupling algorithm.

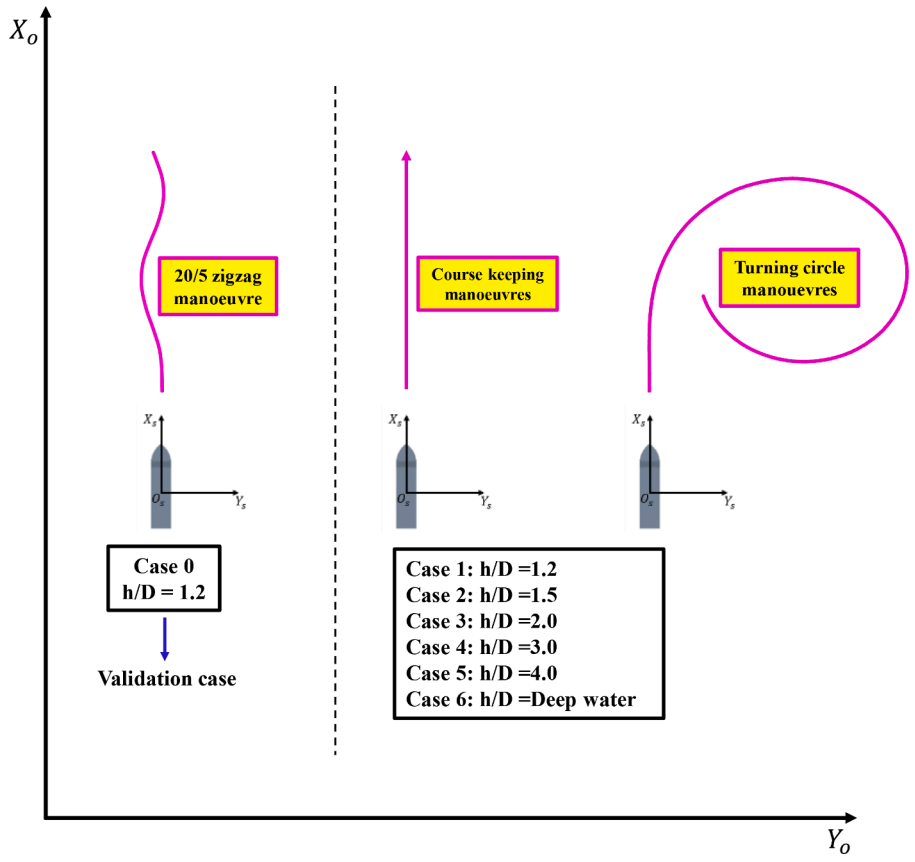

Fig. 3. Schematic views of the simulation cases applied to this study.

2.2.2. Body-force method

A ship propeller was modelled through an actuator disk of finite thickness based on the body force method, in which both axial and tangential body forces are distributed in the flow field within the disk to simulate propeller effects. The ship model used in this work is equipped with a right-handed propeller of which rotation direction is clockwise when propelling the vessel forward as viewed from the ship's stern. In the present simulations, the direction in which thrust is produced by the disk model was determined in accordance with the characteristic of the right-handed propeller. The thrust and torque generated by the actuator disk is dependant on the thrust and torque coefficients K_T and K_Q selected from the propeller performance curve as a function of the advance ratio J ($J = V_{ship} / nD$, where V_{ship} represents the velocity at the propeller location, n is the rotation rate, D is the propeller diameter). V_{ship} was calculated in this study as the volume-averaged velocity over the inflow velocity plane which is located upstream of the actuator disk to consider the actual velocity field at the propeller position. The open water curves produced by MARIN (SIMMAN, 2020) were fed as input variables into the disk model to mimic the KCS propeller performance used in the experiment of the 20/5 zigzag manoeuvre (Case 0). Once the thrust and torque are determined for the operating advance ratio, a uniform volume forces $\mathbf{f_b}$ distribution over the cylindrical actuator disk is prescribed as follows:

$$f_{bx} = A_x r^* \sqrt{1 - r^*} \tag{4}$$

$$f_{b\theta} = A_\theta \frac{r^* \sqrt{1 - r^*}}{r^*(1 - r_h'') + r_h''} \tag{5}$$

$$r^* = \frac{r'' - r_h''}{1 - r_h''}, r_h'', \text{and} = \frac{R_H}{R_P}, r'' = \frac{r}{R_P}, \tag{6}$$

in which f_{bx} denotes the body force component in axial direction, $f_{b\theta}$ denotes the body force component in tangential direction, r is the radial coordinate, R_H is the hub radius and R_P is the propeller radius. The constants A_x and A_θ are computed in the following equations, with T, Q, and t_{disk} representing the thrust, the torque, and the actuator disk thickness, respectively.

$$A_x = \frac{105}{8} \cdot \frac{T}{\pi t_{disk}(3R_H + 4R_P)(R_P - R_H)} \tag{7}$$

$$A_\theta = \frac{105}{8} \cdot \frac{Q}{\pi t_{disk} R_P (3R_H + 4R_P)(R_P - R_H)} \tag{8}$$

A propeller model based on the same approach presented herein has been used to successfully resolve the flow field between the ship hull and propeller, as reported in Kim et al. (2021c).

2.2.3. Coordinate systems

In all CFD simulations presented in this paper, four different reference frames were defined in the CFD model performing self-propelled free-running manoeuvres (as shown in Kim et al. (2021c)): *(1) Earth-fixed coordinate ($O_o - X_oY_oZ_o$), (2) Ship-fixed coordinate (o_s - $x_sy_sz_s$), 3) Propeller-fixed coordinate (o_p - $x_py_pz_p$), and (4) Rudder-fixed coordinate (o_r - $x_ry_rz_r$).* The earth-fixed system of reference, with the origin located at point O_o, is considered as an inertial coordinate frame. In the earth-fixed system, the hydrodynamic forces and moments acting on the ship are first computed by solving the governing equations of the fluid flow. Following this, the forces and moments are translated into the ship-fixed system of reference in which the actuator disk forces and moments acting on the ship are added. The ship-fixed frame, which has the origin located at the centre of mass of the ship (CG), follows all 6DOF motions of the ship; the axis o_sx_s is aligned with the ship's longitudinal axis (positive pointing to the bow), the axis o_sy_s is positive towards the starboard and the axis o_sz_s is positive downward, completing a

Table 3
The total cell numbers for the free-running simulations.

Case no.	Total cell number
0 (h /D=1.2)	8,854,466
1 (h /D=1.2)	8,854,466
2 (h /D=1.5)	8,968,119
3 (h /D=2.0)	9,580,662
4 (h /D=3.0)	9,950,540
5 (h /D=4.0)	10,287,254
6 (Deep water)	8,184,125

right-handed orthogonal axis system. In the body-local frame, the governing equations of motion are solved. The linear and angular momentum equations in the ship-fixed reference can be prescribed as follows:

$$\frac{\mathrm{d}(m\mathbf{V})}{dt} = \mathbf{f} \tag{9}$$

$$\mathrm{M_b}\frac{\mathrm{d}\boldsymbol{\omega}}{\mathrm{dt}} + \boldsymbol{\omega} \times \mathrm{M_b}\,\boldsymbol{\omega} = \mathbf{m} \tag{10}$$

in which m represents the mass of body, $\mathbf{V}$ represents the velocity vector of its centre of mass, $\mathbf{f}$ denotes the resultant force vector acting on the ship, $\mathrm{M_b}$ denotes the tensor of moments of inertia in the body-fixed coordinate system, $\boldsymbol{\omega}$ is the angular velocity vector of the body and $\mathbf{m}$ is the resultant moment vector acting on the body. The resultant forces ($\mathbf{f}$) and moments ($\mathbf{m}$) acting on the ship can be expressed as follows:

$$\mathbf{f} = \boldsymbol{F_p} + \boldsymbol{F_\tau} + \boldsymbol{F_g} + \sum^{F_{ext}} \tag{11}$$

$$\mathbf{m} = \boldsymbol{m_p} + \boldsymbol{m_\tau} + \sum^{m_{ext}} \tag{12}$$

with indicating $\boldsymbol{F_p}$ and $\boldsymbol{m_p}$ the pressure force and moment, $\boldsymbol{F_\tau}$ and $\boldsymbol{m_\tau}$ the shear force and moment obtained by solving the flow field and the integration of the pressure and shear stress on the ship hull. $\sum^{F_{ext}}$. and $\sum^{m_{ext}}$. are the external force and moment acting on the ship, respectively, and $\boldsymbol{F_g}$ is the gravitational force exerted at the CG. In the present CFD simulation, the external force and moment are composed of the propeller forces and moments obtained by t body force method. The propeller fixed reference was defined to determine the direction in

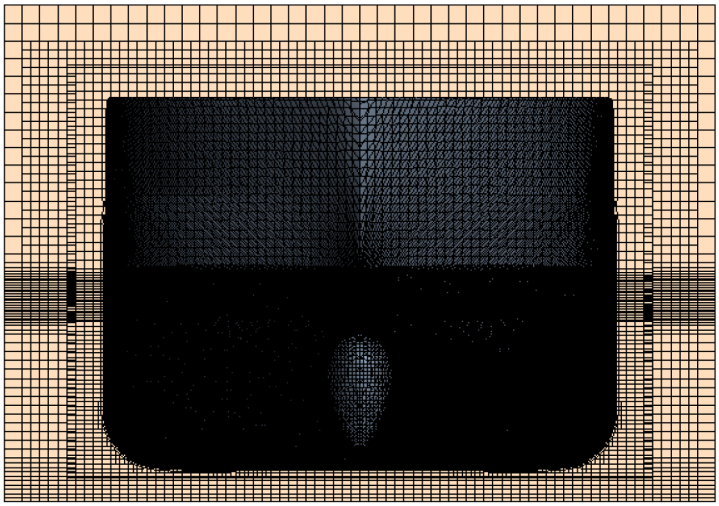

(a) Front view cross-section of the domain

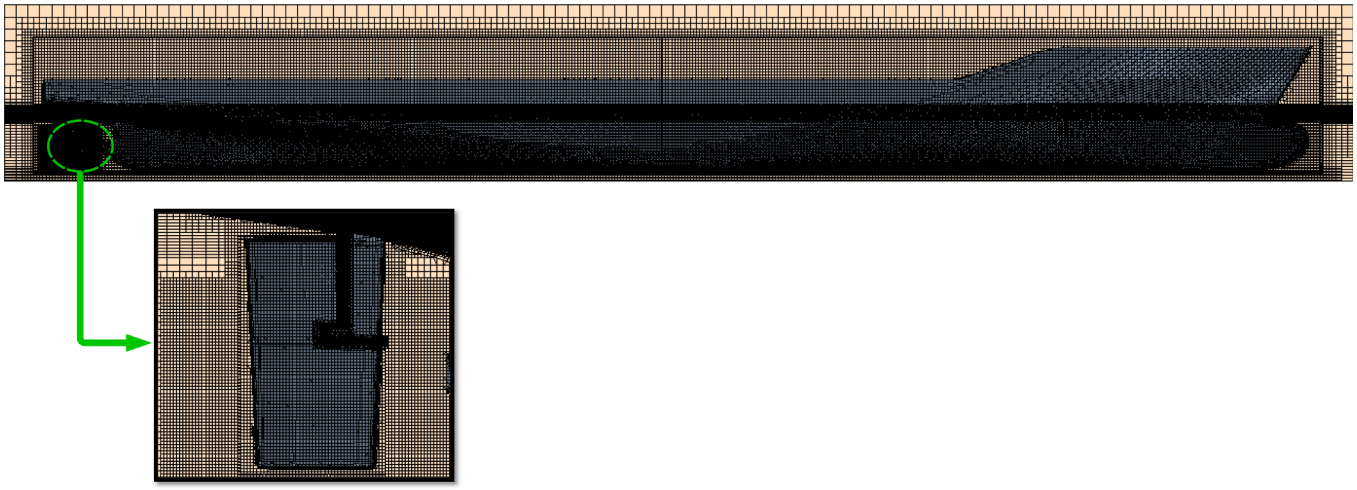

(b) Profile view cross-section of the domain

Fig. 4. Grid structure of the computational domain (Case 0 and 1).

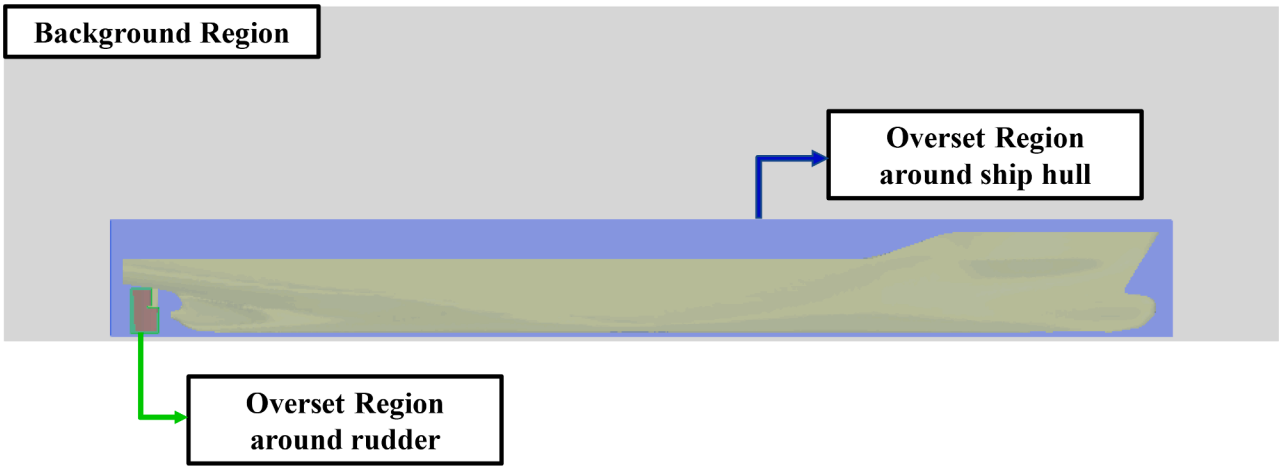

Fig. 5. The schematic of computational domain for the free-running CFD model.

which the actuator disk model produces thrust force, while the rudder-fixed frame was adopted with the aim to control the rudder movement required for the prescribed free-running manoeuvre. In this work, the full 6DOF motions of the free-running ship were simulated using the Dynamic Fluid Body Interaction (DFBI) module, by which the URANS solver calculates the hydrodynamic forces and moments acting on the ship and solves the governing equations of rigid body motion to determine kinematic properties of the ship.

2.2.4. Mesh resolution

The Cartesian cut-cell method was used for the discretisation of the computational domain with the KCS model by means of the automatic meshing facility in STAR-CCM+. In this work, six different grid generations were applied for each free-running simulation; the exact number of grids generated for each case is reported in Table 3. Case 0 and 1 were chosen as representative cases to display a general view of the final computational mesh for the free-running manoeuvre, as illustrated in Fig. 4. With the aim of accurately capturing the complex flow features, the refined mesh density was achieved in the area around the ship hull, the gaps between the rudder and horn, the propeller wake region, and the expected free surface. In particular, a finer grid was created between the bottom of the ship hull and the bottom boundary to ensure the hydrodynamic interaction between the ship bottom and the sea bed appropriately resolved. A prism layer mesh, consisting of orthogonal prismatic cells next to wall surfaces, was also adopted to properly resolve the boundary layer region. The mean flow characteristics (such as pressure, velocity, and separation) inside the boundary layer were approximated by the all-$y+$ wall treatment.

The computational domain for the current CFD model was decomposed into three different regions, as depicted in Fig. 5:1) background region, 2) hull overset region, and 3) rudder blade overset region. A dynamic overlapping grid technique was applied to the latter two regions for the multiple bodies in relative motion (i.e., the ship hull and the rudder blade); by which the full 6DOF motions of the hull and the rudder deflection with respect to the hull can be simulated during the manoeuvres. The advantage of using the dynamic overset approach is that the movement of overset parts with respect to each other can be independently handled without any restrictions. The spacing of the gap part between the rudder blade and the rudder root was slightly adjusted as it was a considerable challenge to simulate the moving rudder due to the tight gap parts which may prevent valid interpolations between the meshes.

2.2.5. Determination of the time step

For all the free-running CFD simulations run in this study, the Courant-Friedrichs-Lewy (CFL) condition was always satisfied during the computations by keeping the CFL number less than unity for numerical stability (Kavli et al., 2017). It is also worth noting that ITTC (2014) recommends the use of $\Delta t \leq 0.01L/U$ for the time step (Δt) selection, with L and U representing ship length and ship speed, respectively. In this work, the time step size for all the simulations was set at $\Delta t = 0.005$s, which is ten times lower than the value obtained from the recommendation presented by ITTC (2014) to gain a reliable level of accuracy for complex phenomena. The use of $\Delta t = 0.005$s has been proved to be reliable in predicting the manoeuvrability of a 1/75.24 scale KCS model (which is the same model scale as that adopted in this work) by performing URANS based simulations, as evidenced in the authors' previous work (Kim et al., 2021c).

2.2.6. Computational domain and boundary conditions

Special care is needed when dealing with the motion of each region. Different motion capabilities were assigned to each computational region for the free-running simulations, which enabled the self-propelled ship to efficiently complete the prescribed manoeuvres in the computational domain with limited size. Without such motion capabilities, the present CFD model would not have been able to achieve a complete manoeuvre in a fixed background region which could not cover the whole course of the manoeuvring ship. In this work, difficulties arising from the limited size of the computational domain were overcome by defining different motions for each computational region. The ship overset region tailored to the ship hull was designed to freely move in full six degrees of freedom according to the DFBI module, while the rudder overlapping region was compelled to follow the ship but can be deflected based on the rudder controller that will be presented in Section 2.3. The motion of the background region was defined to follow the ship motion only with respect to the horizontal plane motions (i.e., surge, sway, and yaw) to enable the free surface to remain within the refined free surface grids during the simulations.

An overview of the computational domain with the imposed boundary conditions is depicted in Fig. 6. When it comes to all the shallow water simulations (Case 0–5) (Fig. 6(a)), the upstream, side, and top boundaries were modelled as a velocity inlet boundary condition which helps to avoid a velocity gradient between the fluid and the wall. The downstream boundary was selected as a pressure outlet. A no-slip wall boundary condition was imposed at the bottom boundary with an aim to represent the presence of the sea floor; in particular, the bottom wall was designed to be stationary with respect to the earth-fixed reference to mimic reality. For the surfaces of the moving bodies (i.e., the hull and the rudder), no-slip wall boundary conditions were applied. It should be stressed that the possible occurrence of wave reflection from the walls was prevented by means of applying the VOF wave damping capability of the software package with a damping length equal to 1.0

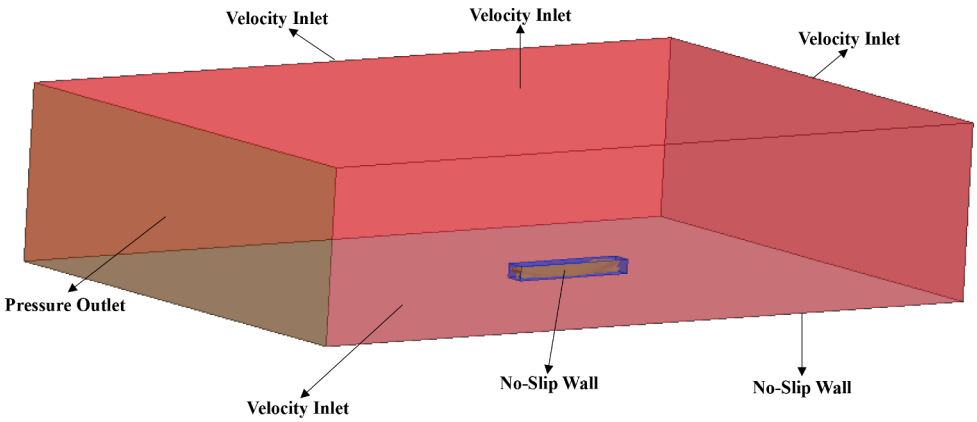

(a) Shallow water simulations (Case 0 – 5)

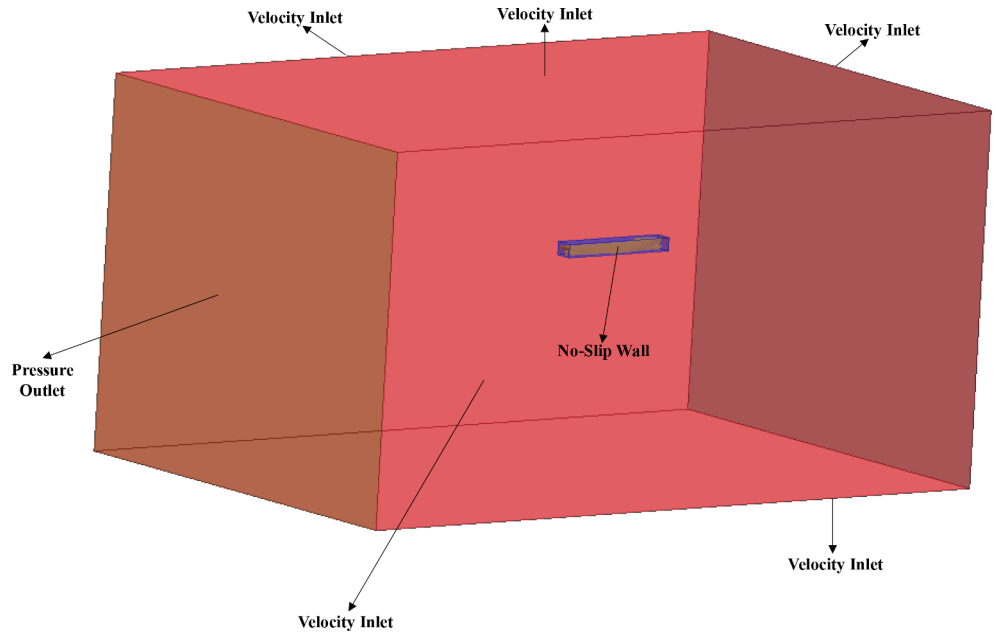

(b) Deep water simulation (Case 6)

Fig. 6. The domain with the applied boundary conditions for shallow and deep water cases.

L_{BP} (~3.06 m.) at the vertical boundaries (i.e., the upstream, downstream, and side walls). For the deep water simulation (Case 6) (Fig. 6 (b)), the only difference from the domain generated to simulate free-running manoeuvres in shallow water is that the bottom boundary was located sufficiently far from the ship and was selected as a velocity inlet to represent deep water conditions.

2.3. Step 3: free running simulations

As was stated in Section 2.1, three different types of ship manoeuvres were performed for the KCS in this work: 1) *20/5 zigzag manoeuvre*, 2) *course keeping control,* and 3) *turning circle manoeuvre*.

As for the modified 20/5 zigzag manoeuvre, the control function is given as follows:

$$\delta(t) = \begin{cases} \min(kt,\ 20),\ \text{1st Rudder Execution} & (t_1 \le t \le t_2) \\ \max(20 - k(t - t_2),\ -20),\ \text{2nd Rudder Execution} & (t_2 \le t \le t_3) \\ \min(-20 + k(t - t_3),\ 20),\ \text{3rd Rudder Execution} & (t_3 \le t \le t_4) \end{cases} \tag{13}$$

in which t denoting the time elapsed after the start of each rudder execution (t_i represents the ith time for rudder execution), $\delta(t)$ the rudder angle, k the maximum rudder rate (k = 20.1°/s). When the ship was advancing forward on a straight course at self-propulsion condition, the rudder blade was first deflected by 20° towards the port side at the maximum rudder rate (1st rudder execution). The ship started to react by turning towards the port side. When the ship heading angle was 5° off the initial course, the rudder was then deflected by 20° towards the starboard side (2nd rudder execution). After the counter rudder angle was applied, the ship initially continued turning to the port with decreasing yaw velocity until it changed sign, so that the ship finally turned to the starboard in response to the rudder deflection. When the

Table 4
Propeller open water test results.

J	CFD			Experiment (MARIN)			Error of K_T (%)	Error of K_Q (%)	Error of η_0 (%)
	K_T	$10K_Q$	η_0	K_T	$10K_Q$	η_0			
0.05	0.427	0.6345	0.053	0.454	0.6686	0.054	5.85	5.10	0.73
0.10	0.418	0.6229	0.106	0.440	0.6501	0.108	4.95	4.18	1.06
0.15	0.407	0.6092	0.159	0.424	0.6302	0.161	3.93	3.33	0.86
0.20	0.394	0.5934	0.211	0.407	0.6088	0.213	2.99	2.52	0.57
0.25	0.381	0.5757	0.263	0.389	0.586	0.264	2.05	1.75	0.25
0.30	0.365	0.5557	0.313	0.370	0.5619	0.314	1.29	1.10	0.06
0.35	0.347	0.5330	0.363	0.350	0.5364	0.364	0.74	0.63	0.25
0.40	0.328	0.5090	0.410	0.329	0.5097	0.411	0.15	0.13	0.03
0.45	0.309	0.4835	0.458	0.308	0.4817	0.457	−0.45	−0.37	−0.28
0.50	0.288	0.4563	0.502	0.285	0.4525	0.501	−1.08	−0.83	−0.28
0.55	0.265	0.4271	0.544	0.262	0.4222	0.543	−1.45	−1.16	−0.32
0.60	0.242	0.3964	0.583	0.238	0.3907	0.582	−1.84	−1.45	−0.33
0.65	0.218	0.3648	0.618	0.213	0.3581	0.617	−2.44	−1.87	−0.28
0.70	0.193	0.3317	0.649	0.188	0.3244	0.647	−2.92	−2.25	−0.44
0.75	0.168	0.2974	0.676	0.163	0.2898	0.671	−3.37	−2.62	−0.79
0.80	0.142	0.2616	0.693	0.137	0.2541	0.686	−4.01	−2.95	−1.10
0.85	0.115	0.2244	0.698	0.111	0.2175	0.688	−4.41	−3.17	−1.55
0.90	0.088	0.1858	0.680	0.084	0.1799	0.669	−5.11	−3.27	−1.75
0.95	0.060	0.1460	0.623	0.057	0.1415	0.610	−5.61	−3.18	−2.20

heading angle reached 5° in the starboard direction, the rudder was reversed again to the port side (3rd rudder execution).

Regarding the course keeping control, the following control module was designed to evaluate the course-keeping capability of the ship:

$$\delta(t) = K_p e(t) + K_i \int_0^t e(t)dt + K_d \frac{de(t)}{dt} \tag{14}$$

$$e(t) = \psi(t) - \psi_c \tag{15}$$

where $\psi(t)$ indicating the instantaneous yaw angle at a given time, ψ_c the target yaw angle which was defined at 0° to keep the ship straight. K_p, K_i, and K_d represent the proportional, integral, and derivative control gains, respectively. For the current CFD model, the control gains were determined by the trial-and-error method ($K_p = 5$, $K_i = 0.05$, *and* $K_d = 3$).

For the starboard turning manoeuvre simulated in the present work, the control mechanism is expressed as follows:

$$\delta(t) = \begin{cases} min(0, -kt), & \delta \geq -35 \\ -35 \end{cases} \tag{16}$$

The above equation suggests that the turning circle manoeuvre executes the maximum rudder deflection (35°) towards the starboard side at the maximum rudder rate; this saturation rudder angle is maintained constant until the completion of the manoeuvre.

2.4. Step 4: results of analysis

Step 4 was to analyse all the simulation results obtained during this study, especially focusing on the dynamic response of the ship and its trajectory in different shallow waters. Throughout all the cases given in Table 2, the proposed approaches discussed in the previous steps of the methodology (Step 1 - 3) were applied to the case studies for the KCS model.

3. Case studies (Results of step 4)

3.1. Verification and validation study

Grid and time-step dependency properties can be estimated by a verification study (i.e., grid-spacing and time-step convergence studies). Due to the high computational cost, however, a verification study has

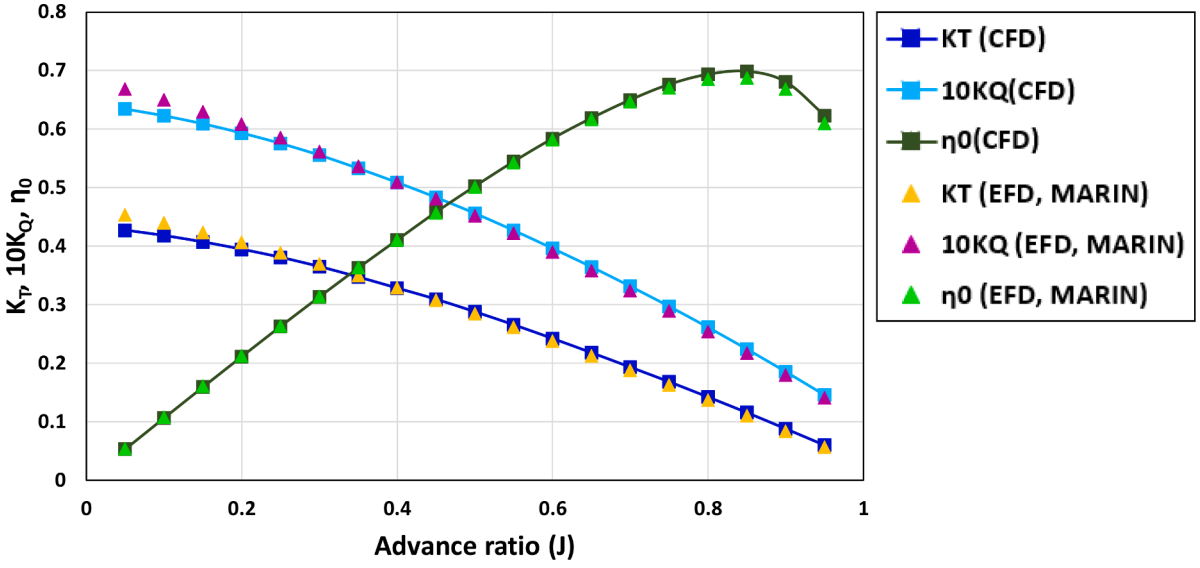

Fig. 7. Propeller open water test results and comparison.

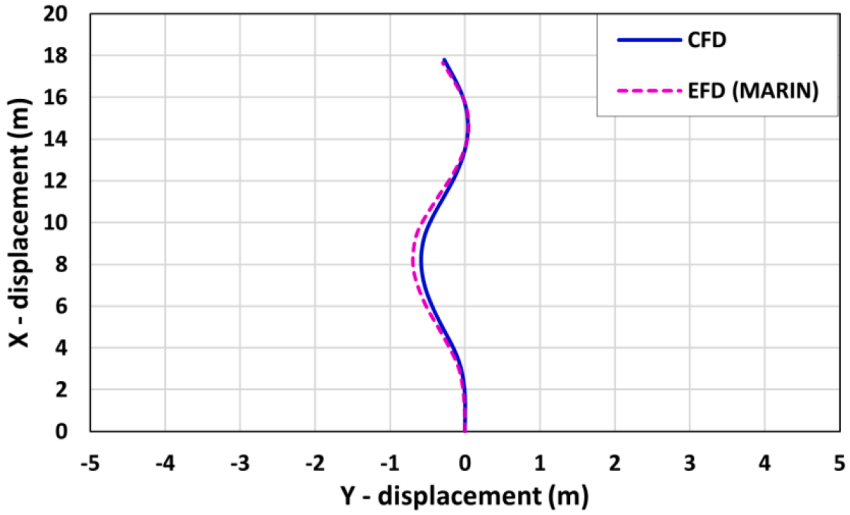

(a) Ship trajectory

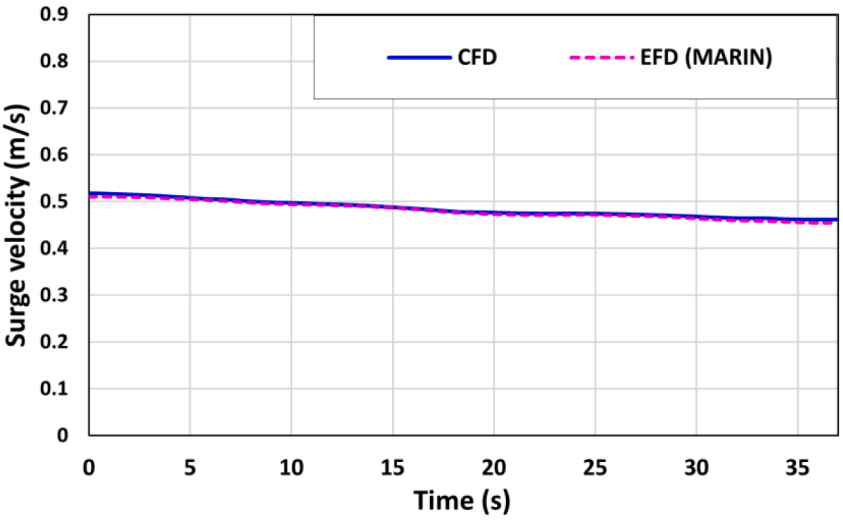

(b) Surge velocity

Fig. 8. The ship trajectory and the time histories of the yaw angle, rudder deflection, and kinematic parameters during the 20/5 modified zigzag manoeuvre in shallow water.

not been performed for the free-running CFD simulations in this work, as has rarely been carried out for free-running simulations by other researchers who used similar numerical approaches in this field (Mofidi and Carrica, 2014; Wang and Wan, 2018; Wang et al., 2018; Liu et al., 2020). In the previous authors' research (Kim et al., 2021c), fortunately, the verification studies of similar manoeuvring problems using the almost same numerical modelling set-up and methodology have been carried out. According to their work, CFD uncertainties for critical turning indices (i.e., the ship advance, transfer, and tactical diameter) were estimated to be a maximum of 0.28% in the spatial convergence study and 0.19% in the temporal convergence study using the grid convergence index method. Monotonic behaviour in a series of grid and time-step uncertainty studies was achieved. The detailed results of the grid and time-step sensitivity studies can be found in Kim et al. (2021c).

The performance of the actuator disk model operating in open water was estimated to ensure the validity of the body force method adopted in this study; to this purpose, an additional simulation was carried out by using the same background grids used for the present free-running simulation (Case 6, deep water) without hull and rudder grids. In Table 4 and Fig. 7, the open water characteristics (thrust coefficients K_T, torque coefficients K_Q, and efficiency η_0 for each advance ratio J) are presented and compared with the available experimental results (SIMMAN, 2020). It can be seen from the table and figure that the agreement between the computed values of K_T, K_Q, and η_0 for the whole range of J and the values provided by the experiments is very good. K_T and K_Q were slightly underpredicted for higher propeller loads, whereas they were slightly overpredicted for lower loads (the errors remained below 6%). Given the fact that a good agreement was achieved between CFD and EFD results, it can be argued that the propeller model based on the body force method demonstrated its robust capability in predicting the propeller performance with regard to thrust and torque; thus, the successive application of this propeller model was made for all the manoeuvring simulations to represent propeller effects.

As was stated in Section 2.1, Case 0 was used for the validation of the present CFD model against the experimental data (SIMMAN, 2020). Fig. 8 presents the simulated ship trajectory and time histories of the ship's speeds, yaw angle, and rudder deflection during the 20/5 modified zigzag manoeuvre in shallow water ($h/D = 1.2$), in comparison with the experimental measurements. In addition to this, the important parameters of the zigzag manoeuvre including overshoot angles were

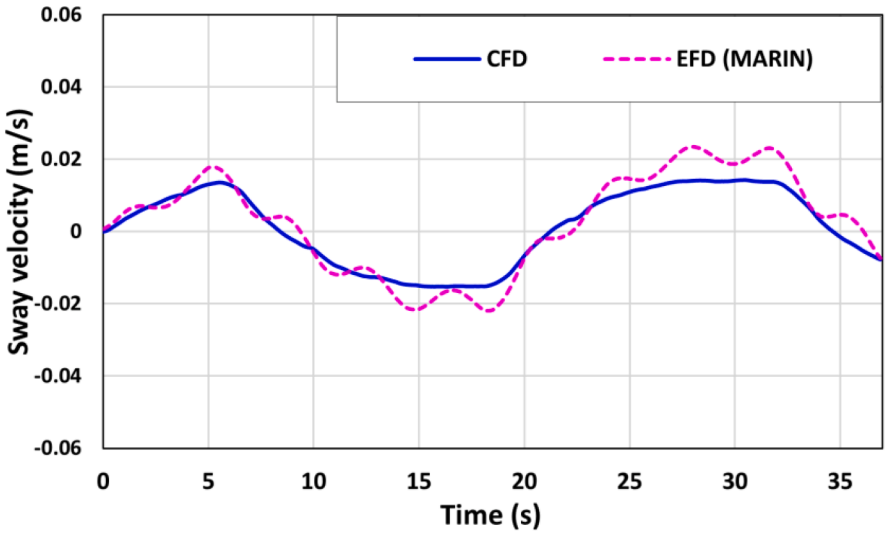

(c) Sway velocity

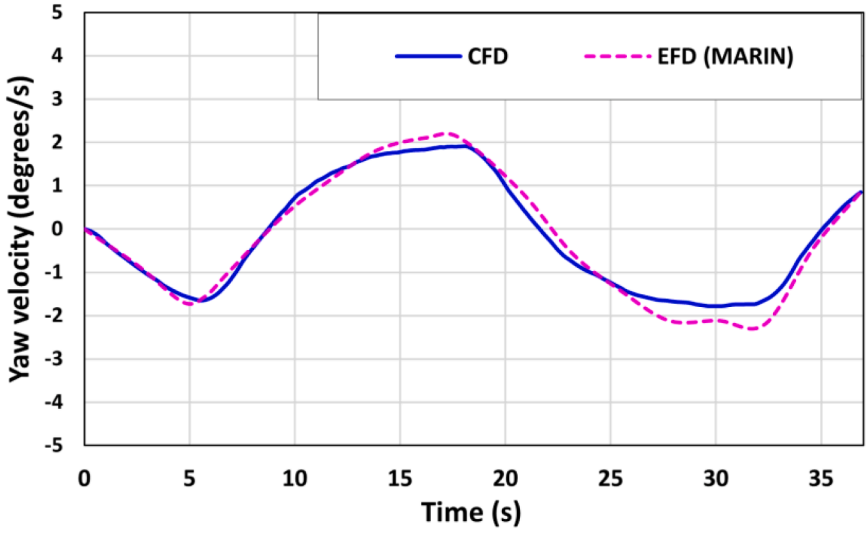

(d) Yaw velocity

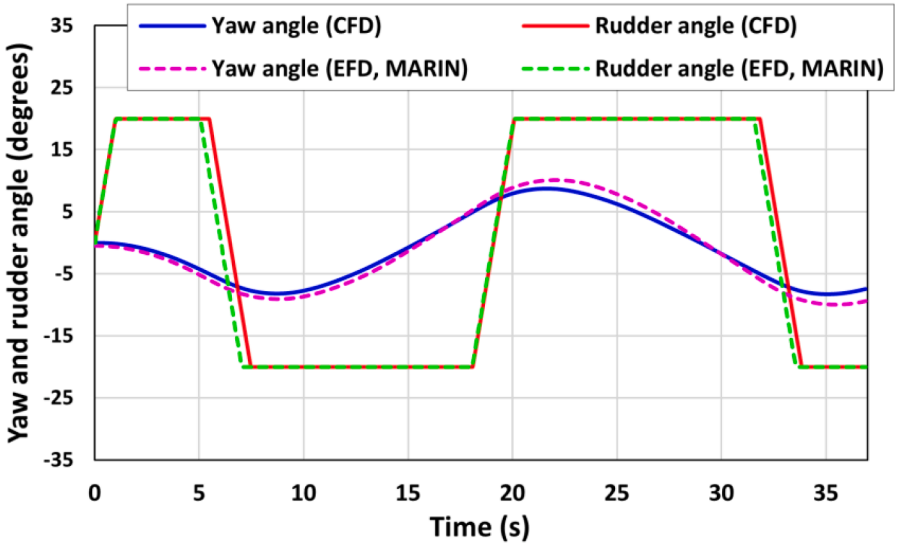

(e) Yaw angle and rudder deflection

Fig. 8. (*continued*).

Table 5
The comparison of the main parameters of the 20/5 zigzag manoeuvre in shallow water (Case 0).

Parameters	CFD	EFD (MARIN) (SIMMAN, 2020)	Error (%)
RPS at self-propulsion point	6.75	6.28	7.48
First overshoot (degrees)	8.18	9.05	−9.61
Second overshoot (degrees)	8.75	10.12	−13.54
Time for the first overshoot (s)	8.73	8.77	−0.46
Time for the second overshoot (s)	21.64	21.99	−1.59

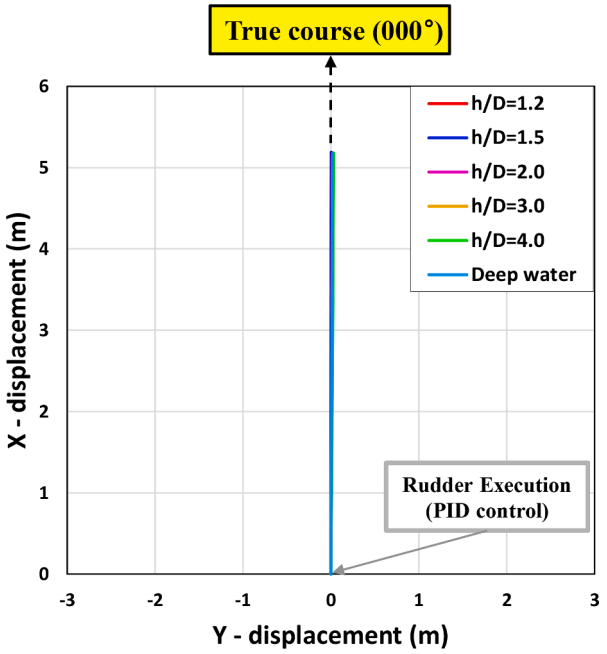

Fig. 9. The comparison of the trajectories experienced by the ship during the course keeping manoeuvre.

reported in Table 5. The CFD predictions of the trajectory experienced by the ship were found in reasonable agreement with the EFD results (Fig. 8(a)), with the minor discrepancy of the ship paths mainly due to the underprediction of the yaw velocity and consequent underestimation of the ship's heading angle. The comparison in terms of the kinematic parameters being composed of the ship velocities in the horizontal plane confirmed the satisfactory agreement between the CFD and EFD results (Fig. 8(b)-(d)). A possible reason why relatively high oscillations are observed in EFD and not in CFD regarding the sway velocity may be associated with the measurement noise during the experiment. As seen in Fig. 8(e) and Table 5, the dynamic behaviour of the ship's heading and rudder deflection was fairly well captured by the present CFD model; the CFD computation underestimated the first and second overshoot angles by 9.6% and 13.5%, respectively. Several possible sources of the discrepancies observed during the manoeuvre between the CFD and experimental results were thoroughly discussed in Carrica et al. (2016), which include variations in initial conditions for yaw angle and yaw velocity, effects of turbulence modelling, effects of neglecting the walls of the tank, the differences in the inertia characteristics between CFD and EFD, etc. Given the acceptable agreement clearly inferred from the figure and table, nevertheless, it can be stated that the validity of the present CFD model has been sufficiently demonstrated, providing a high level of confidence in dealing with the manoeuvring problems in question.

3.2. Course keeping control

From the previous validation case (Case 0), it has been demonstrated that the present free-running CFD model is fairly reliable in predicting the manoeuvring performance of the ship in shallow water, including the ship's trajectory in response to the rudder deflection (closely associated with the course keeping capability). In this sub-section, as a practical application to free-running manoeuvres, the numerical simulations of the course-keeping manoeuvre by the self-propelled ship in shallow water are illustrated.

In general, vessels operating at sea follow the navigation route consisting of different straight-line courses (determined by a master and navigation officers) except when executing ship handling actions to avoid a close-quarters situation or performing planned course alternations. This navigational property underscores the significance of understanding the straight course-keeping capability of vessels; thus, it seems necessary to assess the course keeping behaviours in different environmental conditions in which a ship is to be navigated to ensure safe navigation at sea. The same analysis, performed in the authors' previous studies (Kim et al., 2021a, 2021b, 2021c; Kim et al., 2022; Kim and Tezdogan, 2022) which investigated the course keeping abilities of the KCS in different wave conditions (deep water), was here conducted for the investigation of its steering capabilities in different shallow waters (without any external disturbances).

The computed trajectories experienced by the ship under the course keeping manoeuvres are presented in Fig. 9, in which the location (0,0) of the start of the PID control for course keeping is indicated with a grey arrow. As it can be clearly noticed, all the simulation cases attained good course-keeping control by exhibiting the ship's actual sailing directions almost consistent with the true course (000°). Given the very small deviations from the original course, it was revealed that the finite depths have practically no influence on the course keeping performance in the case of the absence of external disturbances such as winds, waves, and currents. In Fig. 10, the time histories of the yaw angle, rudder deflection, ship resistance, and ship motions during the course keeping manoeuvre are shown. In addition, the mean values of the approach speed, resistance, heave and pitch motions during the manoeuvre are summarised in Table 6. As the predicted ship paths suggest, the ship's heading angles in all cases were maintained to be almost 0°, whilst the rudder deflection angles were largely predicted within a value of 2.0° (a positive rudder angle refers to the direction of rotation to port in agreement with the reference frame adopted in this study). Such small positive rudder angles resulted from an asymmetric flow field induced by the propeller model, which led to the uneven pressure distribution on the rudder surface, as reported in Kim et al. (2021b). This contribution to the small pressure difference exerted a small positive yaw moment, i.e., it turns the ship's heading towards the starboard; as a consequence, the rudder was slightly deflected to the port side according to the PID controller. It is worth noting that the rudder deflection angle may change based on the applied control gains. The effects of the finite depths on the ship resistance were clearly shown in Fig. 10 and Table 6. It was observed that the resistance experienced by the self-propelled ship remarkably increased as the ratio of water depth to draft decreased. This is mainly ascribed to the stronger hydrodynamic interaction between the bottom of the ship and the sea bed in a lower water depth. The ship resistance in shallow water with $h/D = 1.2$ was approximately 59% larger than that in deep water for the same Froude number (Fr=0.095). Regarding the ship motions, only small heave and pitch displacements during the course keeping manoeuvre were numerically observed, stemming from a low approach speed.

In order to visualise the pressure and velocity fields experienced by the ship advancing in shallow water, several zoomed snapshots of the dynamic pressure and longitudinal velocity contours on significant hull cross-sections (see Fig. 11) are displayed in Fig. 12. The sequence of the snapshots (obtained from Case 1) may provide a better insight into the flow evolution along the ship hull. These contours are from the upstream

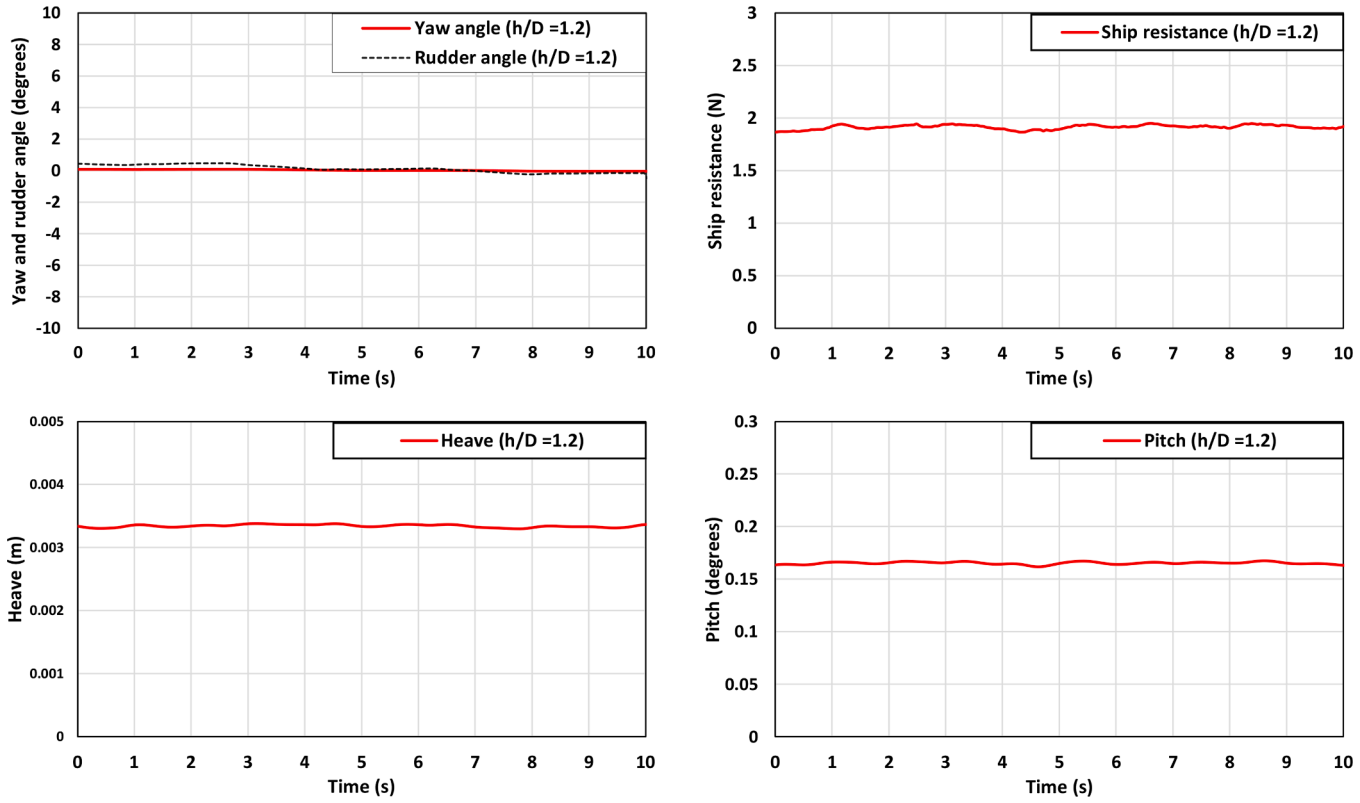

(a) Shallow water (h/D=1.2)

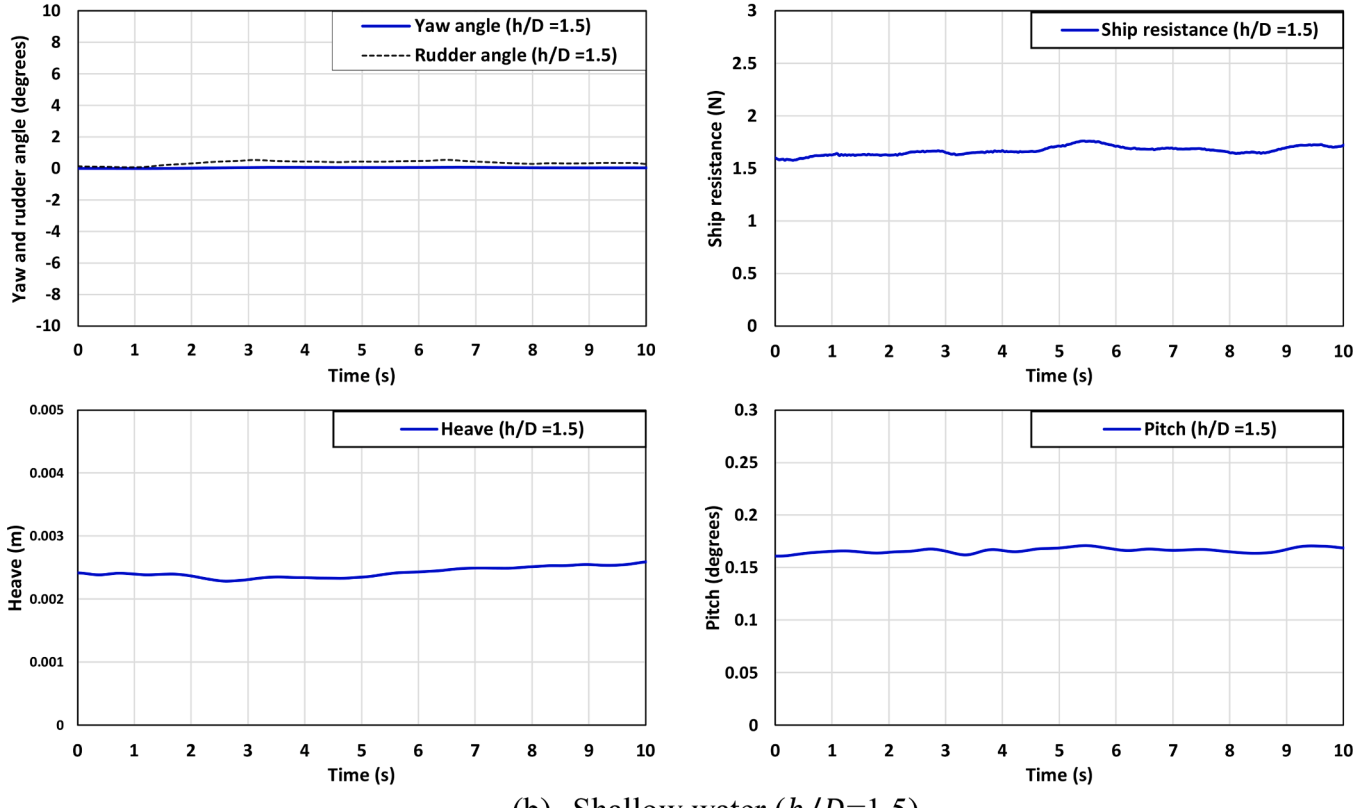

(b) Shallow water (h/D=1.5)

Fig. 10. The time histories of the yaw angle, rudder deflection, ship resistance, and ship motions during the course keeping manoeuvre.

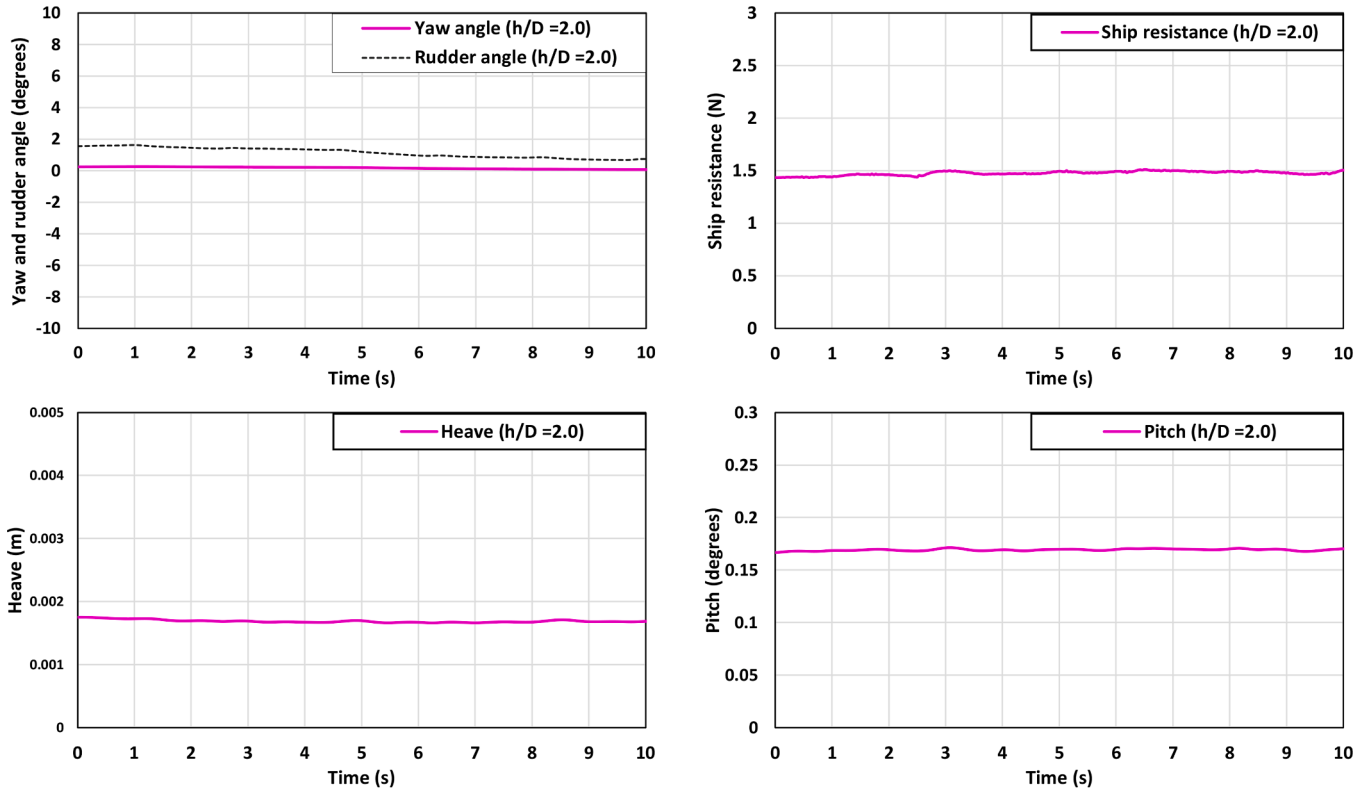

(c) Shallow water (h/D=2.0)

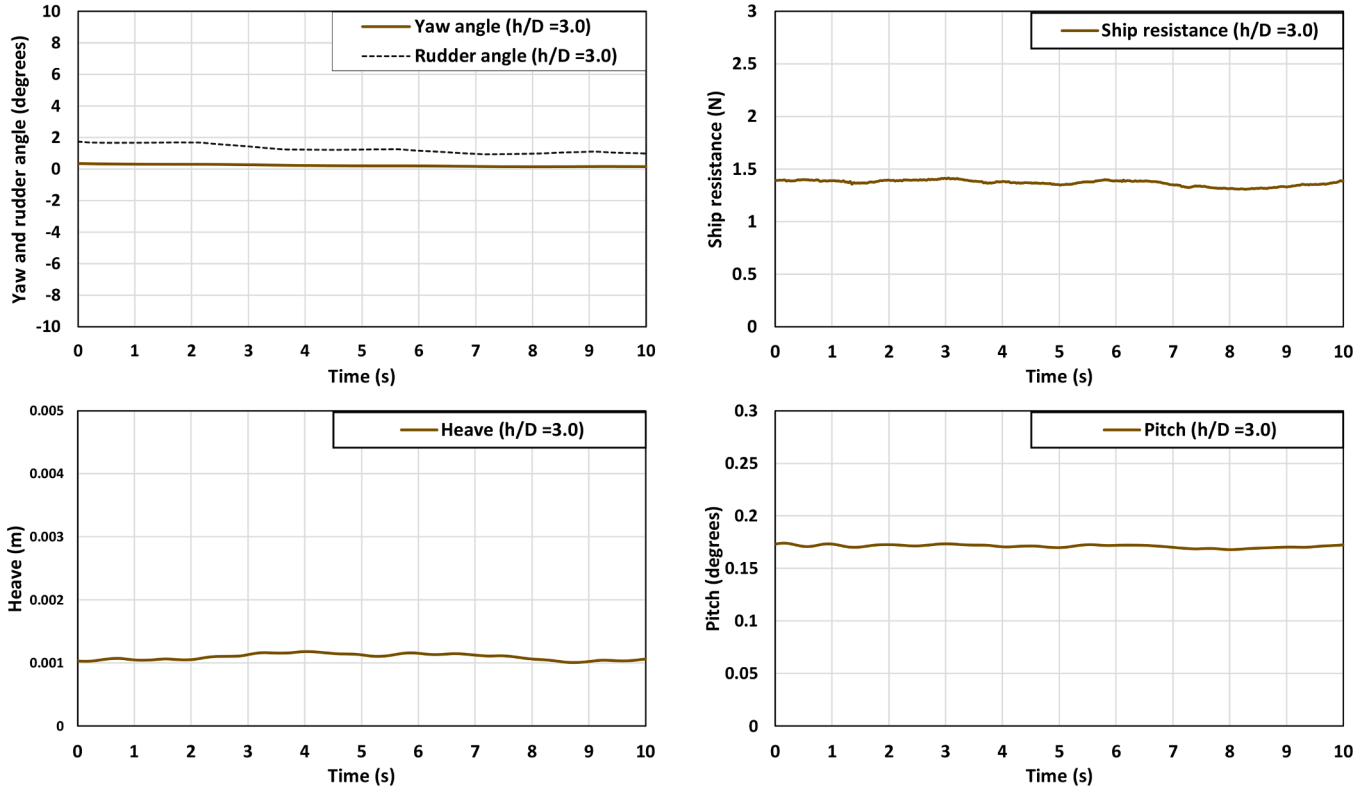

(d) Shallow water (h/D=3.0)

Fig. 10. (*continued*).

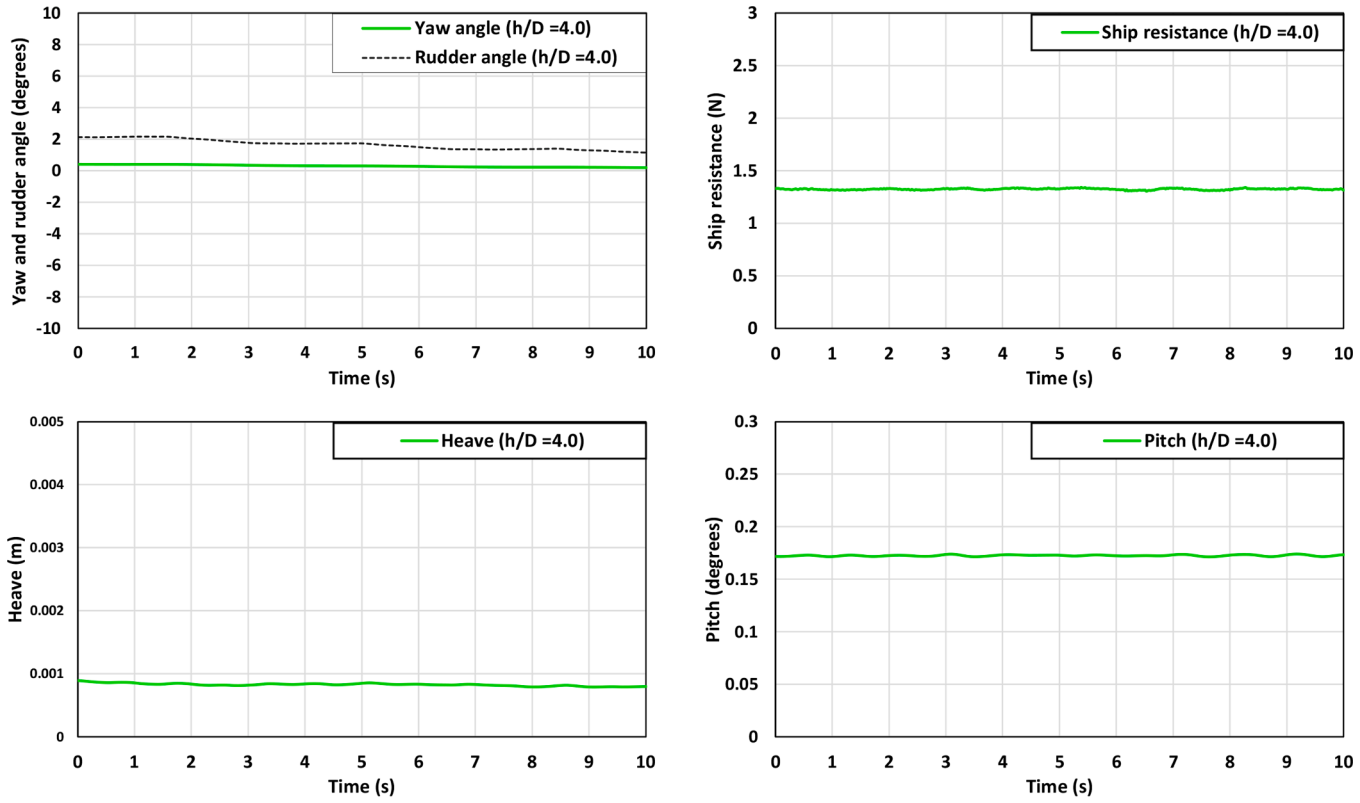

(e) Shallow water (h/D=4.0)

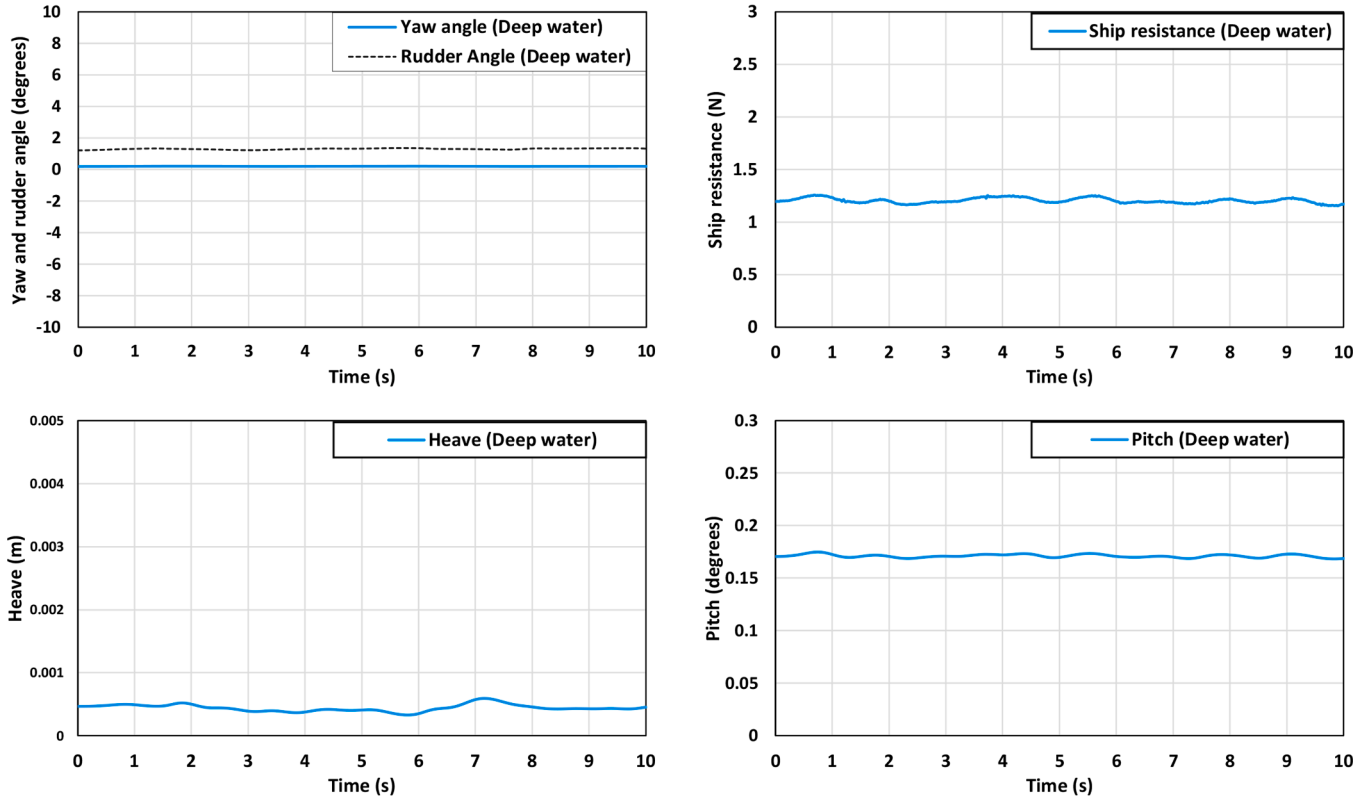

(f) Deep water

Fig. 10. (*continued*).

Table 6
The mean values of the approach speed, ship resistance, heave and pitch motions during the course keeping manoeuvre.

Case no.	Approach speed U_0 (m/s)	Resistance F_x (N)	Heave (m)	Pitch (degrees)
1 ($h/D = 1.2$)	0.518	1.913	0.0033	0.165
2 ($h/D = 1.5$)	0.518	1.669	0.0024	0.166
3 ($h/D = 2.0$)	0.518	1.474	0.0017	0.169
4 ($h/D = 3.0$)	0.518	1.367	0.0011	0.172
5 ($h/D = 4.0$)	0.518	1.323	0.0008	0.172
6 (Deep water)	0.518	1.204	0.0004	0.171

to the downstream of the ship ($-0.492 \leq X/L_{PP} \leq 0.327$). As it can be inferred from Fig. 12, no noticeable hydrodynamic effects caused by the presence of the finite depth was observed at the bow ($X/L_{PP}=0.327$). At the midship section ($X/L_{PP}=0.000$), a negative pressure field was formed, and the flow velocity increased between the bottom of the hull and the sea floor. It was then observed that the ship boundary layer was interacted with the sea bed at $X/L_{PP}=-0.327$ due to the progressive evolution of the boundary layer thickness along the hull. The snapshots reported in Fig. 12(d) (where the flow reached the propeller, $X/L_{PP}=-0.468$) confirmed the disturbed flow fields because of the interaction between the turbulence produced by the boundary layer and the swirl induced by the propeller with the bottom surface. In addition, the pressure and velocity fields became more complicated at $X/L_{PP}=-0.485$ and -0.492 due to the inclusion of the flow around the rudder in the slipstream of the propeller.

3.3. Turning circle manoeuvre

This sub-section will systematically investigate the turning capability of the self-propelled KCS model in different shallow waters; by comparison with the ship's inherent turning ability in deep calm water. Following this, the effects of the finite depths on the manoeuvring performance will be analysed. In the standard turning circle manoeuvre, the ship was sailing forward on a straight course at self-propulsion condition and the rudder was deflected to the hard-over angle (35°, towards the starboard side) at the maximum rudder rate (20.1°/s). Then, the ship started to turn in the starboard direction as a reaction to the rudder deflection. The free-running simulations stopped when the variation of the ship heading angle reached 360° according to the general procedure put forward by IMO (2002). The total simulation running time of each case was different due to the different yaw velocities experienced by the ship during the manoeuvre. As traditionally adopted in ship manoeuvring, the turning behaviours of the ship were assessed in terms of the turning parameters such as the ship advance, transfer, tactical diameter as well as time to 90°/180° heading angle changes.

The predicted trajectories experienced by the ship during the turning circle manoeuvre are depicted in Fig. 13, in which the ship paths are expressed with respect to the earth-fixed coordinate. In the figure, the origin (0,0) of the earth-fixed frame is taken as the position at which the rudder was executed for the turning manoeuvre. The results of the manoeuvring parameters are also reported in Table 7, with an aim to quantify the turning quality of the ship for each simulated case. The contribution of the finite depth to the turning performance of the ship can be found, as clearly evidenced by the noticeable differences in the turning trajectory. In particular, the ship performing the manoeuvre in the shallow waters with $h/D = 1.2$, 1.5, and 2.0 exhibited poorer turning ability when compared to the ship's inherent turning performance in deep water. Despite the same approaching speed (Fr = 0.095), the ship showed significantly larger increases in the tactical diameters (Fig. 13 and Table 7). This was mainly attributed to the insufficient Under Keel Clearance (UKC, the vertical distance between the bottom of the ship and the sea floor), resulting in the strong hydrodynamic interaction between the hull, propeller, and rudder with the sea bed and consequently causing substantial changes in the turning performance of the ship. It was found that when the ship performing the turning manoeuvre, the smaller the UKC, the greater the ship turning diameter can be. Interestingly, the ship manoeuvring in the shallow waters with $h/D = 3.0$ and 4.0 showed a similar tendency to the ship's turning performance in deep water, confirming the weakened effect of the shallow water on the ship's manoeuvrability when h/D is greater than 3.0.

Considering the fact that only small heave, pitch, and roll motions during the turning manoeuvre were observed (mainly due to the absence of waves), the ship's motions in the horizontal plane – surge, sway, and yaw motion – were found decisive for the critical turning indices. As discussed in Kim et al. (2021c), the greater the surge velocity and the longer time taken for the 90° turn, the larger the ship advance and transfer can be. In **Fig. 14**, the time histories of the ship velocities, forces and moments, and drift angles during the manoeuvre were presented for all cases (each case is indicated with a different colour). It appeared from Table 7 that the ship advance and transfer mainly increased with the decrease in the ratio of water depth to draft (h/D) since the ship in smaller h/D ratios experienced the larger surge velocity and the smaller yaw rate during the manoeuvre (**Fig. 14**). The differences in the ship advance and transfer were not significant between the $h/D = 3.0$, 4.0 and deep-water conditions, which may be closely associated with the weakened shallow water effects on the manoeuvrability (despite the slightly different propeller revolution rates). The tactical diameters experienced by the ship also followed the similar trend.

The lateral force of the rudder was observed to rapidly increase soon after the deflection of the rudder blade (due to the increased angle of attack of the rudder), producing a large yaw moment to turn the ship's bow towards the starboard side (**Fig. 14**(g) and (f)). Subsequently, the

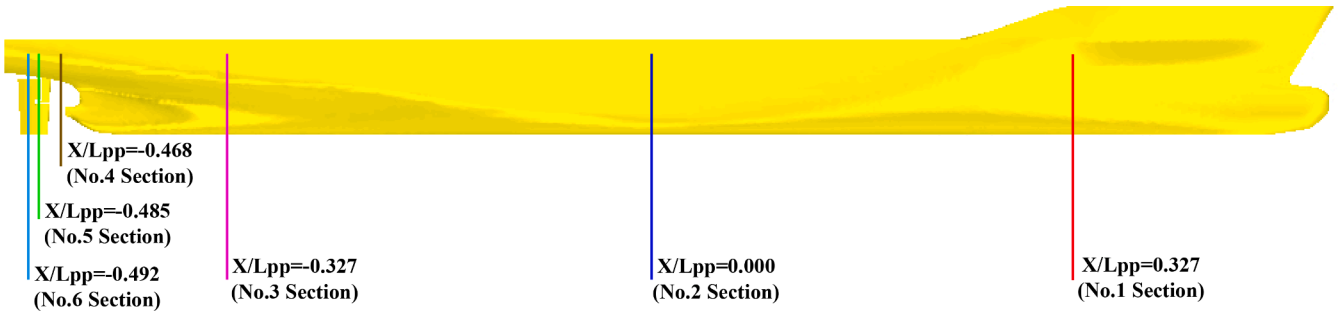

Fig. 11. The location of the cross-sections along the ship at which pressure/velocity fields were obtained.

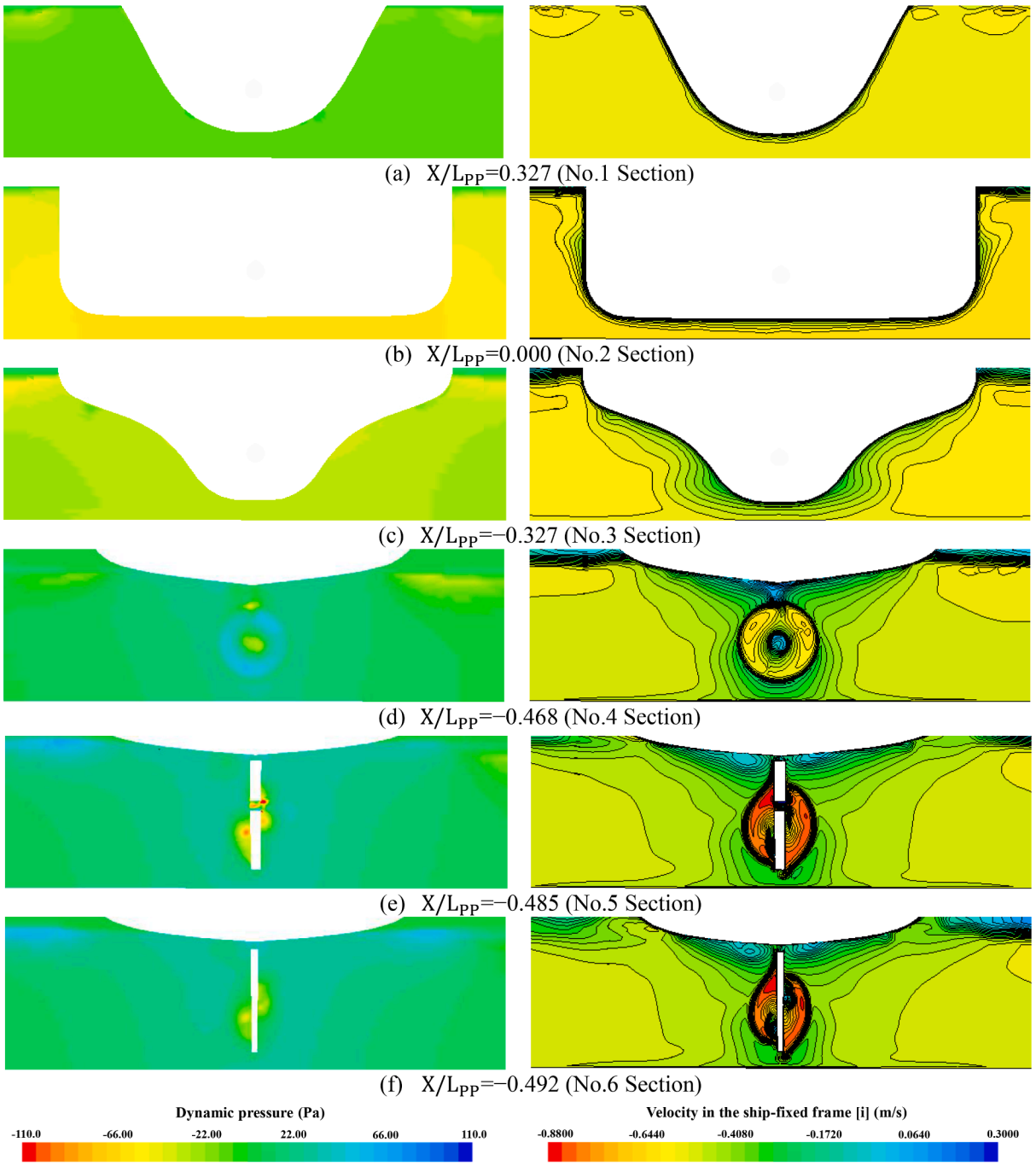

Fig. 12. Dynamic pressure and longitudinal velocity fields during the course keeping manoeuvre on several cross-sections; left: pressure fields and right: velocity fields.

mean effective angle of attack of the rudder decreased as the ship started to turn, and thus the rudder normal force gradually decreased and converged to a certain value. It was found that the rudder normal force was larger in smaller h/D ratios during the steady phase of the turn, being ascribed to the shallow water effects and different propeller rotational speeds. The manoeuvring ship exhibited an involuntary speed loss in the transient phase of the turn as the ship resistance increased with an increase in the drift angle experienced by the ship (Fig. 14(a), (b), and (h)). The speed loss was found larger in deeper depths. The speed loss rate between the initial surge velocity and the minimum value was estimated at 57% for the $h/D = 1.2$, 64% for the $h/D = 1.5$, 68% for the $h/D = 2.0$, 70% for the $h/D = 3.0$, 71% for the $h/D = 4.0$, 72% for the deep-water condition. Despite the larger later force of the rudder in smaller h/D ratios, the ship experienced the smaller sway and yaw velocities during the manoeuvre, implying the poorer turning performance in shallow water (Fig. 14(c) and (e)). It is worth noting that the dynamic behaviours of the vessel in higher h/D ratios became progressively similar to those in deep water, mainly due to the weakened shallow water effects on the ship manoeuvrability.

The comparison of the thrust and torque predicted by the body force method during the manoeuvre is shown in Fig. 15. As stated previously, the performance of the propeller is highly dependant on the volume-averaged velocity over the inflow velocity plane (located upstream of the actuator disk), determined by the complicated interaction between the propeller revolution rate, the presence of the sea floor, and the wake distribution. It can be seen that right after the rudder deflection, the

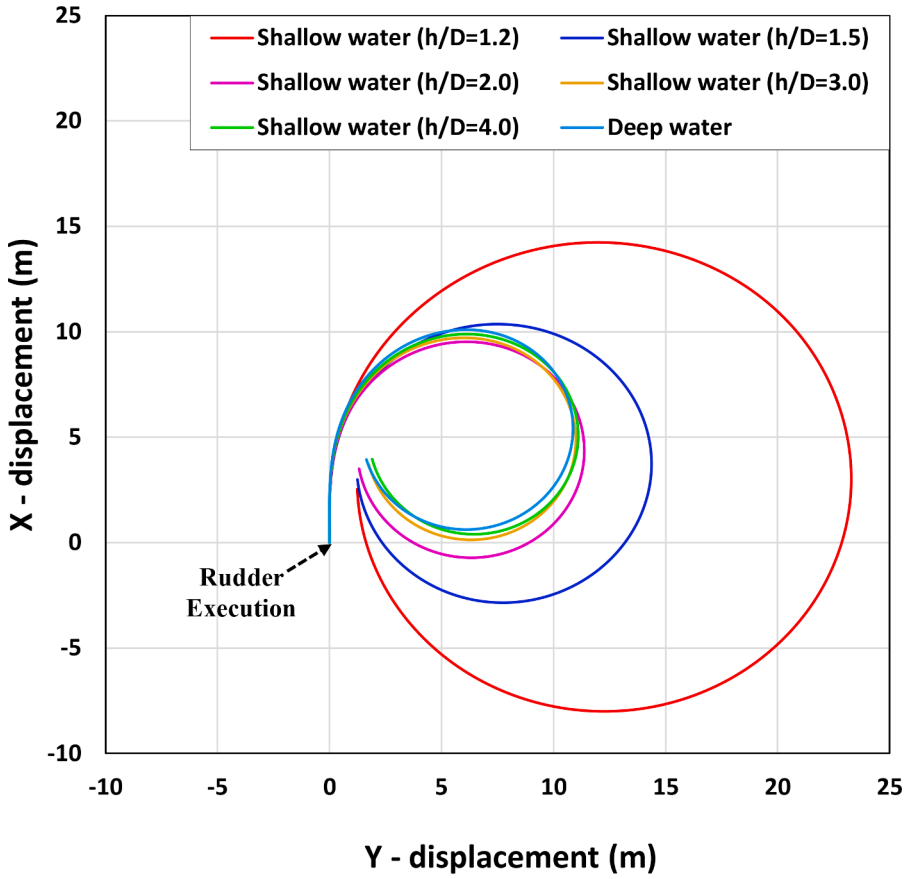

Fig. 13. The predicted turning trajectories for all cases.

Table 7
CFD results: turning parameters.

Parameters (CFD results)	Case 1 (h/D = 1.2)	Case 2 (h/D = 1.5)	Case 3 (h/D = 2.0)	Case 4 (h/D = 3.0)	Case 5 (h/D = 4.0)	Case 6 (Deep)
Advance (m)	14.23 (**4.66L_{BP}**)	10.33 (**3.38L_{BP}**)	9.45 (**3.09L_{BP}**)	9.57 (**3.13L_{BP}**)	9.73 (**3.18L_{BP}**)	9.89 (**3.24L_{BP}**)
Transfer (m)	11.56 (**3.78L_{BP}**)	6.82 (**2.23L_{BP}**)	5.16 (**1.69L_{BP}**)	4.80 (**1.57L_{BP}**)	4.80 (**1.57L_{BP}**)	4.65 (**1.52L_{BP}**)
Time for yaw 90° (s)	47.24	32.51	27.97	27.64	27.92	28.04
Tactical diameter (m)	23.28 (**7.62L_{BP}**)	14.34 (**4.69L_{BP}**)	11.29 (**3.69L_{BP}**)	10.85 (**3.55L_{BP}**)	10.94 (**3.58L_{BP}**)	10.67 (**3.49L_{BP}**)
Time for yaw 180° (s)	93.88	64.51	55.38	54.49	54.78	55.21

thrust and torque developed by the actuator disk slightly increased, being ascribed to the decrease in the advance ratio (due to the increased flow velocity in the disturbed flow region by the rudder activation). Subsequently, the thrust and torque started to decrease because of the increase of the advance coefficients caused by the rapid increases in the sway and yaw velocities experienced by the ship (Fig. 14(c) and (e)). After the ship experienced the peak values for the sway and yaw velocities, the advance ratio gradually decreased mainly due to the speed drops (including the surge velocity) and converged to a certain value in the steady phase of the turn. Accordingly, the propeller underwent a gradual increase in thrust (and torque) and then converged. It was also found that the propeller in smaller h/D ratios developed higher loads during the manoeuvre, closely associated with shallow water effects and different propeller revolution rates. Interestingly, the thrust and torque developed by the disk model during the steady phase of the turn for Case 1 were similar to those in the straight-ahead condition (the self-propulsion condition), whereas the propeller loads during the steady turn were larger than the self-propulsion condition for Case 2–6. This phenomenon resulted from the speed loss rate experienced by the ship during the manoeuvre.

In Fig. 16, the time histories of the heave, pitch, and roll motions experienced by the ship during the turning manoeuvre were presented. From the figure, it clearly appeared that only small ship motions were estimated during the manoeuvre mainly due to the slow approach speed and the absence of external disturbances. Given the available UKC, the predicted heave and pitch motions may not pose a significant threat to navigational safety at sea. In addition, the roll angles for all cases remained below about 1° during the manoeuvre due to a rather weak rudder normal force (compared to the design condition, Fr=0.26).

Case 1, 2, and 3 were selected as representative cases to display pressure and velocity fields during the turning manoeuvre. Fig. 17 shows the close-up views of dynamic pressure and longitudinal velocity fields at X/L_{PP}=−0.485 (No. 5 section) and pressure distributions on the rudder at self-propulsion, maximum yaw rate and steady yaw rate during the turning manoeuvre. It can be seen from the figure that the flow field experienced by the manoeuvring ship in shallow water was characterised by the interactions of the hull wake, boundary layer, propeller, vortex, and sea floor. As the ship started to turn, the vortex was generated by the cross-flow velocity and was convected towards the leeward side due to the yaw-drift motion (clearly evidenced in Fig. 17, maximum yaw rate). The vortex convected away from the hull was strongly interacted with the hull boundary layer, the propeller, and the

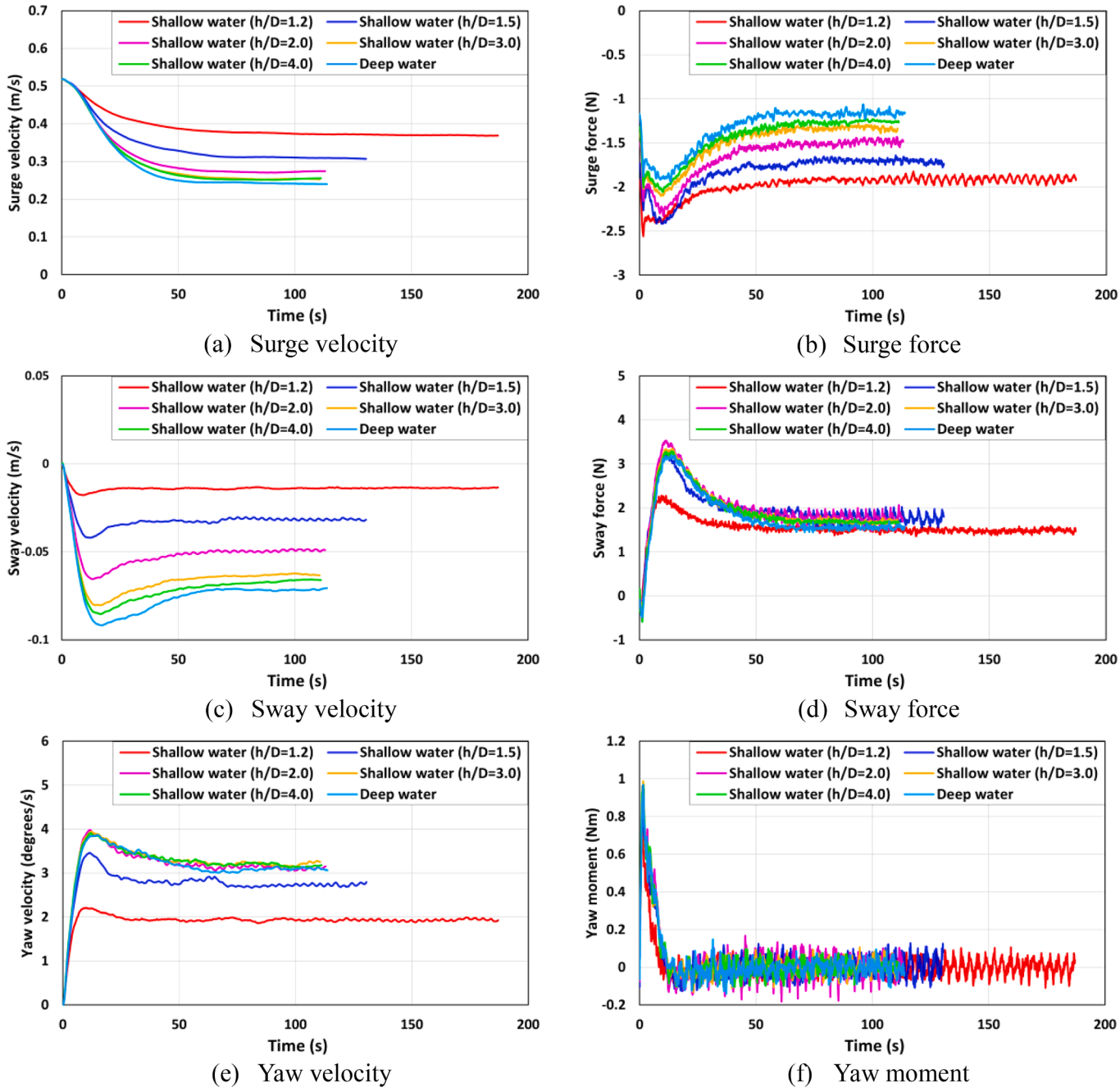

Fig. 14. The time histories of the ship velocities, forces and moments, and drift angles during the standard turning circle manoeuvre.

sea floor, demonstrating the complexity of the resulting flow field. It appeared that this vortex was more weakened in deeper depths. Besides, the vortex observed in the transient phase of the turn was more intense than that in the steady phase. As it can be inferred from the figure, the advancing ship at the self-propulsion condition experienced the uneven pressure distribution between the starboard and the port of the rudder blade due to the asymmetric flow (the swirl) generated by the propeller. The swirl induced by the propeller was directed from the starboard to the port at the bottom of the rudder, resulting in the pressure difference between the starboard and the port of the rudder. After the rudder deflection, the pressure differences were remarkable between the starboard and the port, causing the strong rudder lateral force to turn the ship during the manoeuvre.

The effects of shallow water on the turning performance of a ship is briefly explained by Yeo et al. (2016), who conducted free-running model tests for the KVLCC2 in different shallow waters (h/D = 1.2, 1.5, and 2.0), as follows:

- The change in the ship's heading angle during turning manoeuvres was found slower in relatively shallower water depths
- The hydrodynamic forces experienced by the ship performing turning manoeuvres were observed to increase exponentially with the decrease in the ratio of water depth to draft
- It was also found that the turning parameters such as the ship advance, transfer, and tactical diameter tend to increase in smaller h/D ratios

It has to be mentioned that the numerical results obtained from the

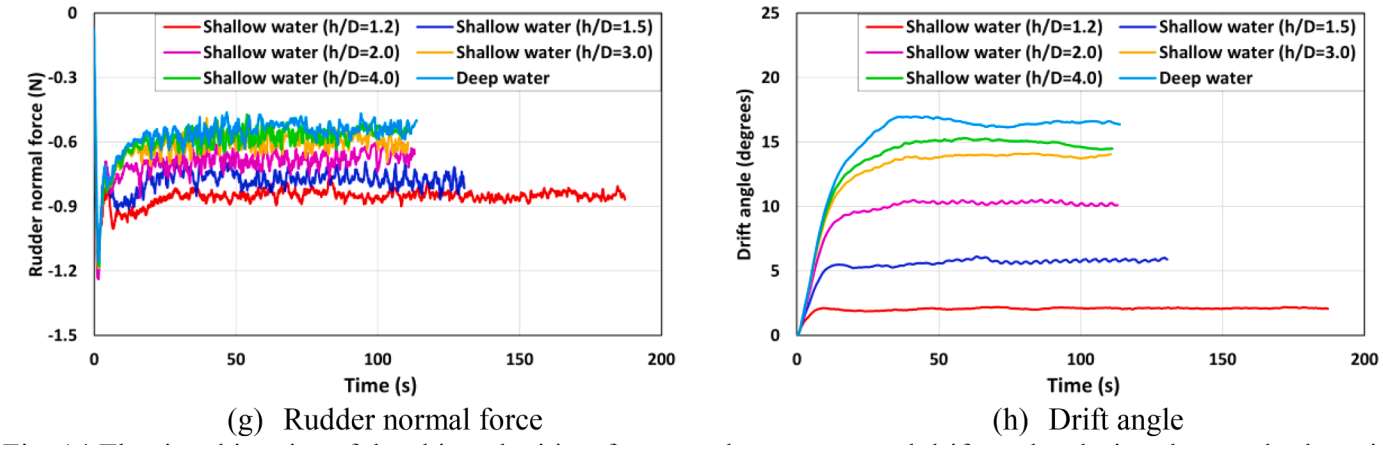

Fig. 14. (*continued*).

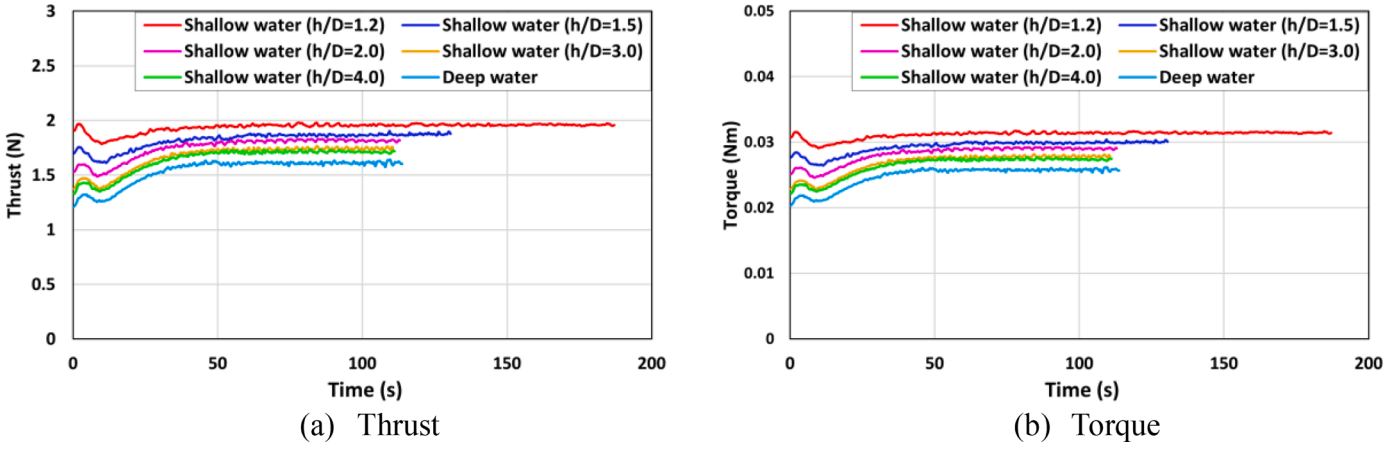

Fig. 15. The time histories of the propeller characteristics during the turning manoeuvre.

present study showed consistent trends with the experimental findings of Yeo et al. (2016).

4. Conclusions and discussion

The present study has demonstrated the effectiveness of the direct CFD model to predict the manoeuvring performance of a container ship (the KCS model) in shallow water using an unsteady Reynolds Averaged Navier-Stokes solver.

As can be seen from the literature survey presented in Section 1, the past studies devoted to free-running CFD simulations are insufficient to offer a comprehensive explanation for the ship manoeuvrability in shallow water. In other words, the previous studies published in this field have mostly focused on the investigation of a ship's manoeuvrability in deep waters; their findings may be inconclusive on the various hydrodynamic phenomena occurring during manoeuvres in shallow water. Thus, this paper aims to add a sound value by analysing the manoeuvrability of the ship (i.e., course keeping and turning manoeuvres) in different shallow water performing free-running CFD simulations.

The free-running model for the prediction of ship manoeuvrability in shallow water has been developed by means of an unsteady RANS solver. The detailed description of the numerical setup adopted for the free-running CFD simulations was given in Section 2 (for example, propeller modelling, mesh generation, time step selection, treatment of computational region motions). The proposed CFD model has demonstrated an acceptable level of accuracy and reliability in estimating the manoeuvring behaviour of the ship in shallow water. The comparisons with the available free-running model experiments have been satisfactory in terms of both kinematic and trajectory parameters (Case 0). Considering that there are no definite recommendations/guidelines regarding the numerical setup of the free-running CFD simulation in shallow water, it is believed that this paper could encourage academic researchers to participate in research on manoeuvring problems in shallow water performing free-running CFD simulations without much difficulty.

In addition, this model has allowed to analyse the different manoeuvring properties of the ship in question, i.e., course-keeping and turning circle manoeuvres. Although the results obtained from this study are for a specific benchmarking ship, the results could be applicable to a conventional container vessel of similar type and dimensions. The key findings of this study can be summarised as follows:

1) As long as the course keeping capability of the ship is concerned, the manoeuvring ship in different shallow waters attained good course-keeping control as supported by the ship's actual sailing directions consistent with the true course. This aspect underscores that the finite depths have practically no influence on the course keeping ability in the case of the absence of external loads.
2) Regarding the turning manoeuvre, the contribution of the finite depth to the turning behaviour of the ship has been emphasised in comparison with the critical turning parameters and hydrodynamic quantities in relation to h/D ratios. It was revealed that the ship advance, transfer, and tactical diameter mainly increased with the

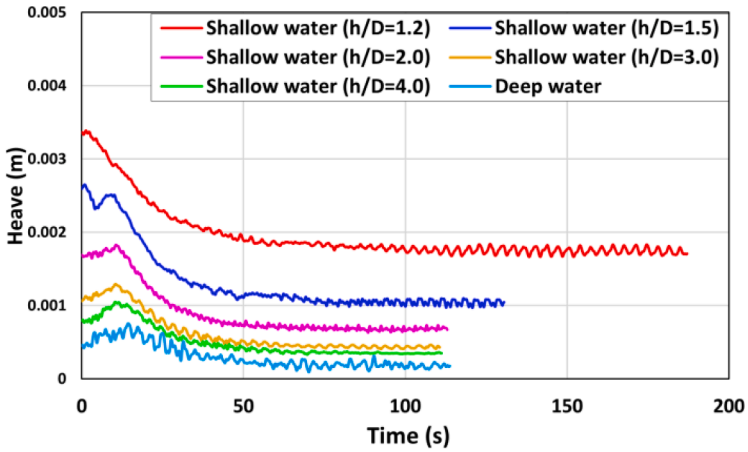

(a) Heave

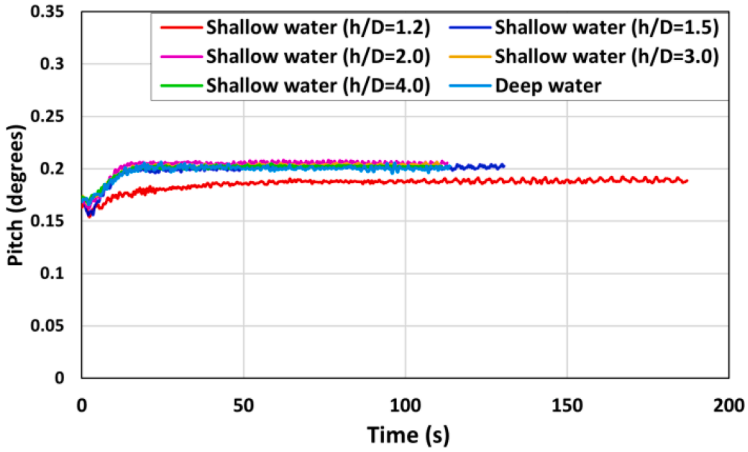

(b) Pitch

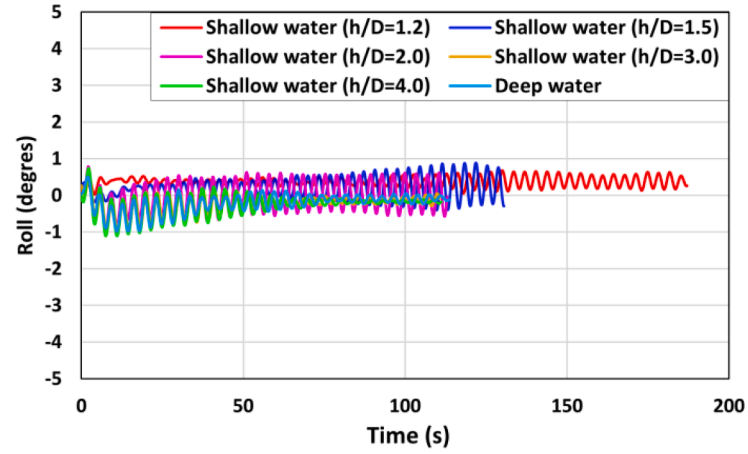

(c) Roll

Fig. 16. The time histories of the ship motions during the turning manoeuvre.

decrease in the ratio of water depth to draft. The predicted transfer and tactical diameter for the h/$D = 1.2$ are more than twice as large as those for the deep-water condition, for the same approach speed (Fr = 0.095). It has to be pointed out that the differences in the turning parameters were not significant between the h/$D = 3.0$, 4.0, and the deep-water condition, which may stem from the negligible contribution of shallow water to the manoeuvring performance of the ship in these particular water depths.

3) The involuntary speed loss in the transient phase of the turn was found larger in deeper depths as the ship resistance increased with an increase in the drift angle experienced by the ship. The speed loss rate between the initial surge velocity and the minimum value was predicted at 57% for the h/$D = 1.2$, 64% for the h/$D = 1.5$, 68% for the h/$D = 2.0$, 70% for the h/$D = 3.0$, 71% for the h/$D = 4.0$, 72% for the deep-water condition.
4) The principal properties of the flow field experienced by the manoeuvring ship were also analysed, confirming the complicated interactions between the hull wake, boundary layer, propeller, vortex, and sea floor.

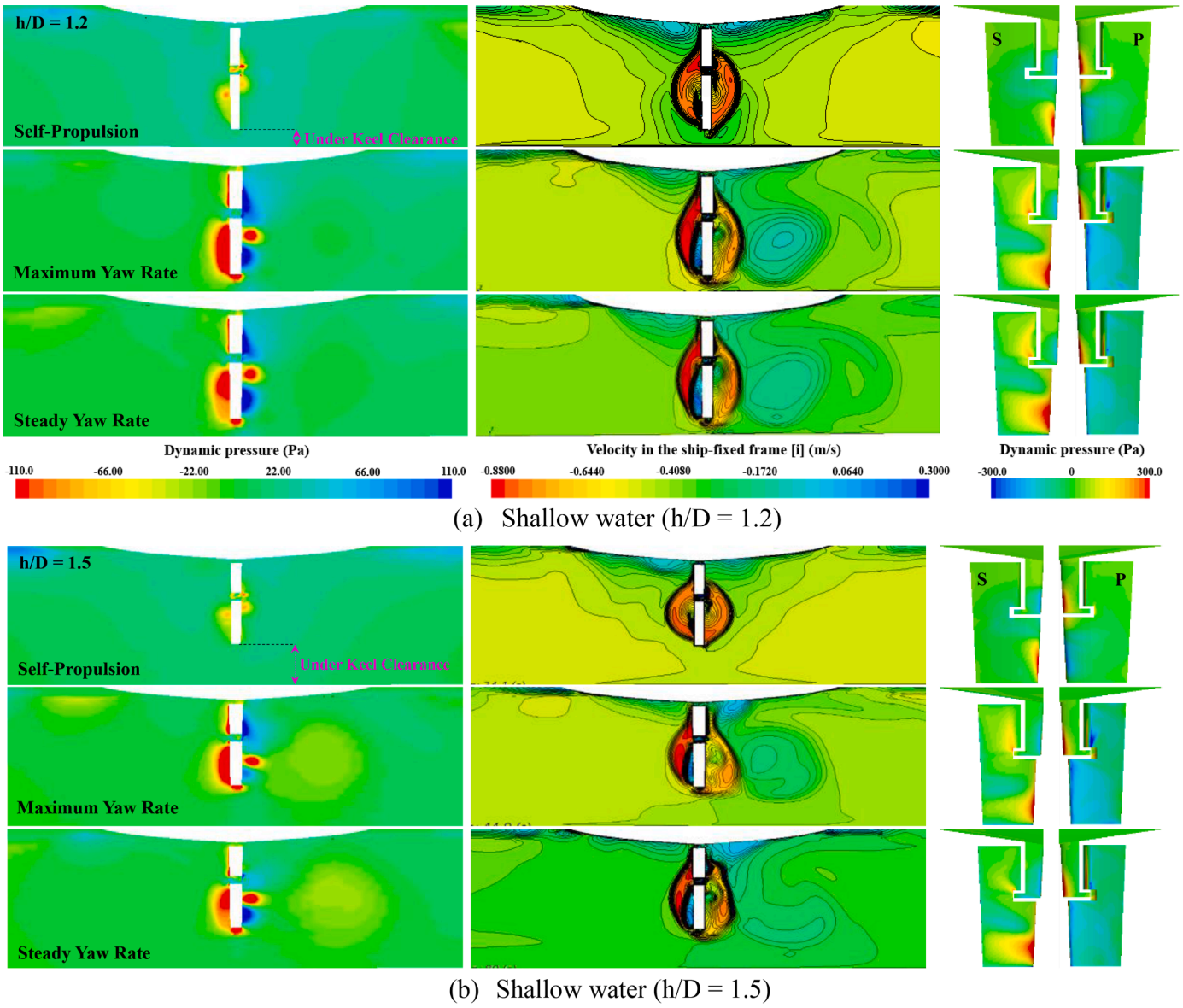

Fig. 17. The close-up views of dynamic pressure and longitudinal velocity fields at X/L_{PP}=−0.485 (No. 5 section) and the pressure distributions on the rudder (S: starboard profile, P: port profile) at self-propulsion (top), maximum yaw rate (centre) and steady yaw rate (bottom) during the turning manoeuvre (obtained from Case1, 2 and 3).

It should be borne in mind that unsuitable ship handling actions taken by navigating officers can result in navigational casualties such as contact, collision, and grounding (EMSA, 2020). Taking into account the shallow water effect which is significant on ship manoeuvrability, it is thought that masters and navigation officers who are in charge of ship handling should fully understand the manoeuvring capabilities of a ship in shallow water for proper decision-making about ship manoeuvring actions. In this regard, this research will contribute to enhancing navigational safety at sea, providing a clear and detailed insight into ship manoeuvrability in shallow water.

In connection with a rapidly growing interest in autonomous navigation, the importance has been stressed of the correct prediction of ship manoeuvrability in a real seaway (i.e., course keeping and turning capabilities). Autonomous or remote-controlled ships should be capable of operating independently based on an autonomous navigation system that adequately controls the rudder and propeller with an aim to maintain its intended course or avoid collision. Safe autonomous operation can be achieved through the accurate prediction of the manoeuvring performance of a ship, enabling the ship to maintain its desired trajectory during a given operation. With this point of view, the CFD-based ship manoeuvring analyses adopted in this study could offer a comprehensive and detailed insight into ship manoeuvrability in shallow water, providing a valuable contribution to the improvement of autonomous navigation systems.

According to the European funded Project SHOPERA (Sprenger et al., 2016), it was revealed that finite depths have a notable effect on propagating wave properties. Given this, this study should be extended to incorporate different wave conditions as ship manoeuvrability will be strongly dependant on not only shallow water effects but also incident wave conditions. With the Stokes wave model, further study into the manoeuvring performance of the ship in waves with shallow water could be made.

CRediT authorship contribution statement

Daejeong Kim: Writing – original draft, Conceptualization, Methodology, Formal analysis, Investigation, Validation, Visualization, Data curation. **Tahsin Tezdogan:** Conceptualization, Methodology,

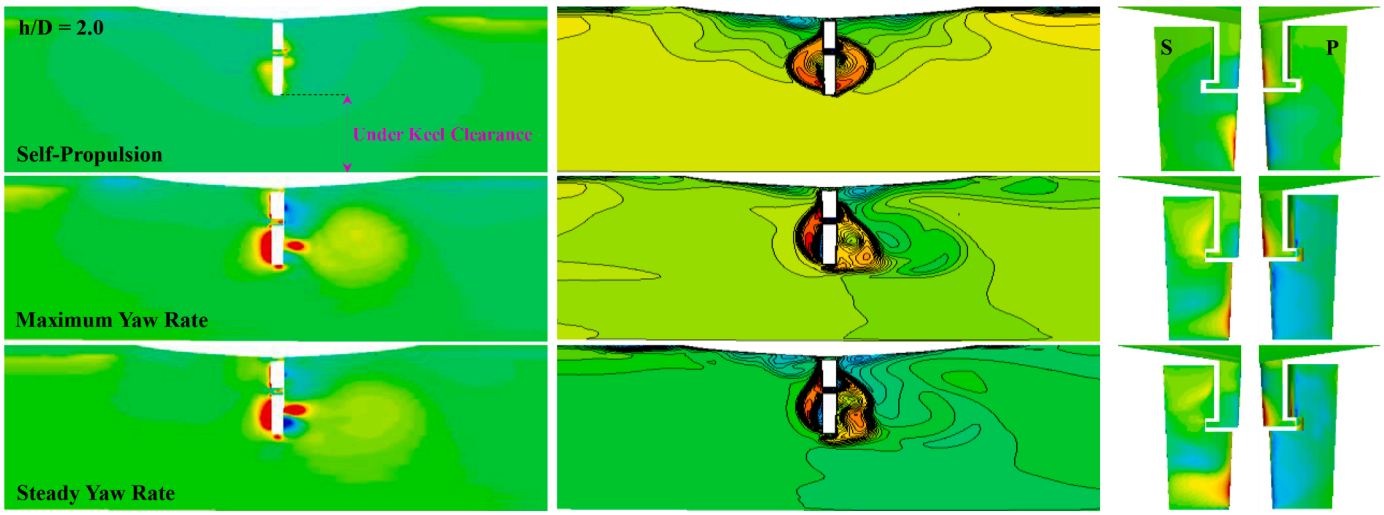

(c) Shallow water (h/D = 2.0)

Fig. 17. (*continued*).

Supervision, Writing – review & editing, Resources, Supervision. **Atilla Incecik:** Supervision, Writing – review & editing, Resources, Supervision.

Declaration of Competing Interest

The authors declare that they have no known competing financial interests or personal relationships that could have appeared to influence the work reported in this paper.

Acknowledgements

It should be noted that the results were obtained using the ARCHIE-WeSt High Performance Computer (www.archie-west.ac.uk) based at the University of Strathclyde.

References

Abkowitz, M.A., 1964. Lectures on ship hydrodynamics–Steering and manoeuvrability.
Broglia, R., Dubbioso, G., Durante, D., Di Mascio, A., 2015. Turning ability analysis of a fully appended twin screw vessel by CFD. Part I: single rudder configuration. Ocean Eng. 105, 275–286.
Carrica, P.M., Mofidi, A., Eloot, K., Delefortrie, G., 2016. Direct simulation and experimental study of zigzag maneuver of KCS in shallow water. Ocean Eng. 112, 117–133.
Dubbioso, G., Durante, D., Di Mascio, A., Broglia, R., 2016. Turning ability analysis of a fully appended twin screw vessel by CFD. Part II: single vs. twin rudder configuration. Ocean Eng. 117, 259–271.
EMSA, 2020. Annual Overview of Marine Casualties and Incidents 2020.
Hasanvand, A., Hajivand, A., 2019. Investigating the effect of rudder profile on 6DOF ship turning performance. Appl. Ocean Res. 92, 101918.
Hirt, C.W., Nichols, B.D., 1981. Volume of fluid (VOF) method for the dynamics of free boundaries. J. Comput. Phys. 39 (1), 201–225.
IMO, 2002. Explanatory Notes to the Standards For Ship Manoeuvrability.
IMO, 2014. 2013 Interim Guidelines for Determining Minimum Propulsion Power to Maintain the Manoeuvrability of Ships in Adverse Conditions.
Inoue, S., Hirano, M., Kijima, K., Takashina, J., 1981. A practical calculation method of ship maneuvering motion. Int. Shipbuild. Progress 28 (325), 207–222.
ITTC, 2002. The Specialist Committee On Esso Osaka - Final Report and Recommendations to the 23rd ITTC.
ITTC, 2014. ITTC - Recommended Procedures and Guidelines: Practical Guidelines For Ship CFD Applications.
ITTC, 2017. Tasks and Structure of 29th ITTC Technical Committees and Groups (version 4).
Kavli, H.P., Oguz, E., Tezdogan, T., 2017. A comparative study on the design of an environmentally friendly RoPax ferry using CFD. Ocean Eng. 137, 22–37.
Kim, D., Song, S., Jeong, B., Tezdogan, T., 2021a. Numerical evaluation of a ship's manoeuvrability and course keeping control under various wave conditions using CFD. Ocean Eng. 237, 109615.
Kim, D., Song, S., Jeong, B., Tezdogan, T., Incecik, A., 2021b. Unsteady RANS CFD simulations of ship manoeuvrability and course keeping control under various wave height conditions. Appl. Ocean Res. 117, 102940.
Kim, D., Song, S., Sant, T., Demirel, Y.K., Tezdogan, T., 2022. Nonlinear URANS model for evaluating course keeping and turning capabilities of a vessel with propulsion system failure in waves. Int. J. Naval Archit. Ocean Engin. 14, 100425.
Kim, D., Song, S., Tezdogan, T., 2021c. Free running CFD simulations to investigate ship manoeuvrability in waves. Ocean Eng. 236, 109567.
Kim, D., Tezdogan, T., 2022. CFD-based hydrodynamic analyses of ship course keeping control and turning performance in irregular waves. Ocean Eng. 248, 110808.
Lee, S., Hong, C., 2017. Study on the course stability of very large vessels in shallow water using CFD. Ocean Eng. 145, 395–405.
Liu, C., Wang, J., Wan, D., 2020. CFD Simulations of Self-Propulsion and Turning Circle Maneuver up to 90° of Ship in Waves. J. Ship Res. 1–14.
Liu, Y., Zou, Z., Zou, L., Fan, S., 2019. CFD-based numerical simulation of pure sway tests in shallow water towing tank. Ocean Eng. 189, 106311.
Menter, F.R., 1994. Two-equation eddy-viscosity turbulence models for engineering applications. AIAA J. 32 (8), 1598–1605.
Mofidi, A., Carrica, P.M., 2014. Simulations of zigzag maneuvers for a container ship with direct moving rudder and propeller. Comput. Fluids 96, 191–203.
Muscari, R., Broglia, R., Di Mascio, A., 2008. Trajectory prediction of a self-propelled hull by unsteady RANS computations. In: Proceedings of the 27th ONR Sym- posium on Naval Hydrodynamics. Seoul, Korea.
Papanikolaou, A., Zaraphonitis, G., Bitner-Gregersen, E., Shigunov, V., El Moctar, O., Soares, C.G., Reddy, D.N., Sprenger, F., 2015. Energy efficient safe ship operation (SHOPERA). In: Proc. 6th European Transport Research Conference, Transport Research Arena - TRA 2016, Warsaw, 18-21 April 2016.
Perić, R., Abdel-Maksoud, M., 2018. Analytical prediction of reflection coefficients for wave absorbing layers in flow simulations of regular free-surface waves. Ocean Eng. 147, 132–147.
Shen, Z., Wan, D., Carrica, P.M., 2015. Dynamic overset grids in OpenFOAM with application to KCS self-propulsion and maneuvering. Ocean Eng. 108, 287–306.
Siemens, 2020. Simcenter STAR-CCM+ Documentation.
SIMMAN, 2020. Workshop On Verification and Validation of Ship Manoeuvring Simulation Methods.
Sprenger, F., Maron, A., Delefortrie, G., Cura-Hochbaum, A., Papanikolaou, A., 2016. Experimental studies on seakeeping and manoeuvrability in adverse weather conditions. J. Ship Res.
Tezdogan, T., Incecik, A., Turan, O., 2016. Full-scale unsteady RANS simulations of vertical ship motions in shallow water. Ocean Eng. 123, 131–145.
Toxopeus, S., Simonsen, C., Guilmineau, E., Visonneau, M., Xing, T., Stern, F., 2013. Investigation of water depth and basin wall effects on KVLCC2 in manoeuvring motion using viscous-flow calculations. J. Mar. Sci. Technol. 18 (4), 471–496.
Wang, J., Wan, D., 2018. CFD investigations of ship maneuvering in waves using naoe-FOAM-SJTU Solver. J. Mar. Sci. Appl. 17 (3), 443–458.
Wang, J., Zou, L., Wan, D., 2017. CFD simulations of free running ship under course keeping control. Ocean Eng. 141, 450–464.
Wang, J., Zou, L., Wan, D., 2018. Numerical simulations of zigzag maneuver of free running ship in waves by RANS-Overset grid method. Ocean Eng. 162, 55–79.
Yasukawa, H., Yoshimura, Y., 2015. Introduction of MMG standard method for ship maneuvering predictions. J. Mar. Sci. Technol. 20 (1), 37–52.
Yeo, D., Yun, K., Kim, Y., 2016. Experimental study on the manoeuvrability of KVLCC2 in shallow water. In: 4th MASHCON-International Conference on Ship Manoeuvring in Shallow and Confined Water with Special Focus on Ship Bottom Interaction, pp. 287–294.